Journal of Applied Fluid Mechanics, Vol. 18, No. 3, pp. 678-697, 2025.
Available online at www.jafmonline.net, ISSN 1735-3572, EISSN 1735-3645.
https://doi.org/10.47176/jafm.18.3.2915

Computational Investigation of Fluidic Thrust Vectoring Control in Modified Vikas Nozzle

T. Harish Ragavendra†, P. A. Anupama, K. S. Jai Pranesh, D. Lakshmanan and R. Abinaya

Department of Aeronautical Engineering, Bannari Amman Institute of Technology, Sathyamangalam, Tamil Nadu – 638401, India.

†*Corresponding Author Email: harishragavendra.ae20@bitsathy.ac.in*

ABSTRACT

Over the decades, polar satellite launch vehicles and geosynchronous launch vehicles have utilized variants of the Vikas engine for numerous space operations. The pitching control for those launch vehicles is achieved by gimbaling the Vikas engine nozzle up to ± 4° with mechanical actuating parts. This research investigation dealt with the design modification, analysis, and estimation of performance parameters in the modified Vikas nozzle configurations intended for fluidic thrust vectoring control. Hence, the technique of interest in this investigation was to assess the effects of the fluidic throat skewing technique in an adapted nozzle configuration of the Vikas nozzle. The distinct design configurations were initially iterated with the design of experiments (DOE) method to estimate and adopt an optimum nozzle configuration with higher thrust vectoring effectiveness. The computational analysis utilized the k-ε Reynolds-averaged Navier-Stokes (RANS) numerical model. The flow characteristics of the resolved nozzle configuration were analyzed and validated under three distinct sonic mach freestreams. Finally, air was employed as the secondary fluid in the injector plenum, and the analysis was carried out by varying the secondary mass injection rates. The analysis results depicted that the implemented fluidic injection thrust vectoring approach was significantly effective by achieving ± 5° of tilt with a system thrust force ratio of 0.9190 for 9% of secondary mass flow rate injection.

Article History

Received June 8, 2024
Revised September 16, 2024
Accepted October 1, 2024
Available online January 1, 2025

Keywords:

Computational analysis
RANS based model
Distinct sonic Mach
Throat skewing control
System thrust force ratio

1. INTRODUCTION

The aerospace industry extensively utilizes compressible flow characteristics in aircraft engines, rocketry and various applications. Since 1980s, compressible flow analysis have remained the topic of significant research investigations (Hamid, 1989; Faheem et al., 2021; Lai & Sheng, 2023; Li et al., 2024; Muhammed et al., 2024). Among them, thrust vectoring is a potential technique involving various mechanisms to displace a vehicle's thrust direction. The typical application of a thrust vector system involves flight path correction, vehicle motion control, and tuning of mismatched thrust from the nozzle. In general, the thrust vectoring control in a vehicle is achieved by employing thrust vectoring techniques, namely mechanical actuation thrust vectoring (MATV) and fluidic injection thrust vectoring (FITV). Conventionally, MATV nozzles were found to be integrated with moving mechanical parts. MATV actuation systems were typically adapted with moving jet vanes, reaction control systems, gimballing orbital maneuvering systems, or jet tab based on their design geometry and maneuvering applicational purposes. The investigations conducted by Ikaza (2000), Isaac and Rajashekar (2014) and Yu and Shu (2017); revealed that MATVs are efficient in terms of thrust maneuvering control. It was difficult to find an appropriate thrust vectoring system to produce thrust deflections without compromising its size, weight, and design simplicity. Comprehending the drawbacks of MATV, supersonic FITV methods were considered for further investigation. Eventually, from the computational analysis carried out by Ali et al. (2012), it was observed that FITV nozzles had several advantages over MATV nozzles, such as lower aerodynamic instabilities, a lower weight ratio, and fixed nozzle design geometry resulted in lower mechanical complexities.

Over the past two decades, numerous computational and experimental research investigations were carried out in subsonic, sonic, and supersonic mach operating conditions incorporated with FITV (Deng et al., 2014; Ferlauto & Marsilio, 2017; Schwagerus et al., 2023). The scope of experiments carried out by Deere (2003)

NOMENCLATURE

$\alpha_{i,flap}$	flap injector angle
γ	specific heat ratio of the fluid
δ_β	pitch deflection angle
η	thrust vectoring effectiveness
ρ	static density at the exit
ρ_O	total density of primary flow
A^*	cross sectional area of the nozzle throat
A_{ce}	cross sectional area of the nozzle exit
$a_{i,flap}$	distance of flap injector from throat
A_{ex}	axial exit cross sectional area
A_{ey}	lateral exit cross sectional area
$C_{f,\,g\,sys}$	thrust force ratio of system
$C_{p,\,\beta}$	boattail pressure coefficient
d_1	total length of convergent section of nozzle
F_0	thrust force in non-vectored nozzle
$F_{i,p}$	ideal isentropic nozzle thrust in primary flow
$F_{i,s}$	ideal isentropic nozzle thrust in secondary injected flow
F_R	resultant force
F_x	axial force
F_y	lateral force
H	diameter of convergent section
h_{thr}	diameter of throat section
K_{TC}	resultant thrust coefficient
L_{flap}	total length of divergent section of nozzle
M	Mach number
m_p	mass flow rate of primary flow
m_s	mass flow rate of injected secondary fluid
M_s	Mach number of injected secondary fluid
M_∞	critical Mach number
P_O	total pressure of the primary stream
P	static pressure at the exit
P_{amb}	ambient pressure
P/P_{jt}	ratio of static pressure to total jet pressure
P_e	nozzle area-weighted average exit static pressure
P_s	total pressure of the secondary stream
R_{gc}	gas constant
T_O	total temperature of primary stream
T	static temperature at the exit
Ts	total temperature of the secondary injection
U_{ex}	velocity of x component
U_{ey}	velocity of y component
V	velocity
V_s	average exit velocity

ABBREVIATION

CF	Counter Flow
CFD	Computational Fluid Dynamics
DOE	Design of Experiments
FITV	Fluidic Injection Thrust Vectoring
FTS	Fluidic Throat Skewing
GCI	Grid Convergence Indicator
MATV	Mechanical Actuation Thrust Vectoring
NPR	Nozzle Pressure Ratio
PSLV	Polar Satellite Launch Vehicle
RANS	Reynolds-Averaged Navier-Stokes
SMFR	Secondary Mass Flow Rate
SVC	Shock Vector Control

addressed both positive and negative aspects of different nozzle configurations integrated with FITV techniques such as Counter Flow (CF), Shock Vector Control (SVC), and Fluidic Throat Skewing (FTS) to achieve thrust vectoring in supersonic speeds.

Various research experiments were conducted with the CF technique which involved the suctioning of the primary jet by the secondary jet streams (Flamm, 1998; Miller et al., 2012; Banazadeh & Saghafi, 2017). A vacuum was employed to the plenum, which was then fed to the suction slot, intervening a shrouded collar and the primary nozzle. As a result, the flow near the collar was accelerated, and flow maneuvering was produced due to the pressure drop accumulated in the system (Flamm, 1998; Miller et al., 2012; Banazadeh & Saghafi, 2017). Drawbacks, including hysteresis effects, additional suction supply source requirements, and complexities in airframe integration, were witnessed in CF technique experimentations conducted by Deere (2003) and Wu et al. (2019).

The performance studies performed by Neely et al. (2007), Jingwei et al. (2018), Chen and Liao(2020) and Resta et al. (2021) employed the SVC technique to achieve thrust vectoring and involved forced injection of the secondary fluid stream from the flap section of the nozzle to the supersonic primary flow. The secondary fluid's contact with the supersonic flow was observed to cause an obstruction, leading to the formation of an oblique shock. The research investigation of Deere (2003), Forghany et al. (2017) and Jingwei et al. (2020) demonstrated that losses in thrust performance and thrust vectoring were apparent when the generated oblique shock came into contact with opposing nozzle walls. Maneuvering the primary flow with SVC was less efficient at fully expanded conditions, and the thrust performance losses were high during over-expanded conditions (Deere, 2003; Forghany et al., 2018).

In contrast to other techniques that depend on manipulating shock waves and providing suction slots, the FTS technique occurs with two modes of operation, namely vectoring mode and non-vectoring mode; in the case of non-vectoring mode, the sonic plane is developed in the minimum cross-sectional area of the nozzle. In the vectoring mode, the nozzle throat plane is shifted to a new aerodynamically reduced cross-sectional area with secondary asymmetric fluid injection (Deere, 2003). Flow deflection occurs ahead of the newly created throat in the subsonic region. The subsonic flow deflection can aid in minimizing significant thrust losses. Experimental studies demonstrated that the FTS technique can outperform SVC and CF vectoring methods due to the nozzle's capability to generate a subsonic deflection in the flow (Lim et al., 2006; Miller et al., 2012; Li & Saito, 2012). From the earlier research carried out by Deere (2003) and Miller et al. (2012), it was found that the FTS technique achieved improved overall efficiency than other techniques, and the system's thrust force ratio of the

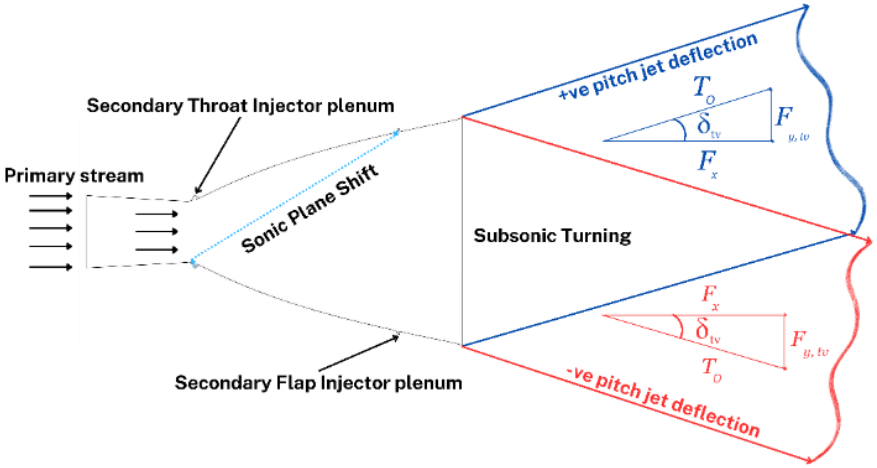

Fig. 1 Fluidic throat skewing implemented in Vikas nozzle geometry

respective nozzles were improved from $C_{f,\ g\ sys}$ = 0.94 to $C_{f,\ g\ sys}$ = 0.98 by having less structural complexity, a higher thrust-to-weight ratio, lower noise levels, and enhanced control stability over the vectoring directions.

Even though various studies (Wu et al., 2021; Salimi et al., 2022;) were performed by employing a secondary injection technique to produce the thrust vectoring actions, analytical and computational research on parametric effects developed during secondary injection needs to be investigated. Research performed by Yagle et al. (2001) and Afridi et al. (2023) addressed FTS-based investigations in various nozzles with their respective design geometry.

Relatively, no research investigation is conducted by incorporating Vikas nozzle configuration with the FITV technique. Hence, further exploration is needed to understand this method and its operation with a real-time nozzle. To carry out the research systematically, the DOE approach proposed by Miller et al. (2012), Jankovic et al. (2021) and Wang et al. (2024) is utilized to determine the efficient Vikas nozzle configuration to investigate the effect of FTS. Initially, the air is employed as a working fluid. The nozzle vectoring performance parameters are analytically and computationally obtained to determine the efficiency of the FTS technique in the configured Vikas nozzle.

2. ANALYTICAL MODELLING OF PERFORMANCE PARAMETERS

When secondary air is introduced into the propelling nozzle, the boundary layer contact with the flow injected and the constrained nozzle flow causes a complex sonic plane shift. Figure 1 depicts the fundamental principle of FTS working implemented in the computational investigation. The nozzle flow condition used in this FTS investigation is considered an isentropic flow for analytical modeling. According to isentropic relations by (Anderson, 2004), the area, temperature, density, and pressure proportions can be represented as follows in Eqs. (1), (2), (3) and (4) respectively,

$$\frac{A_{ce}}{A^*} = 1/M^2 \left[\frac{2}{\gamma+1}\left(1+\frac{\gamma-1}{2}M^2\right)\right]^{\left(\frac{1}{2}\right)[(\gamma+1)/(\gamma-1)]} \quad (1)$$

$$\frac{T_0}{T} = \left(1+\frac{\gamma-1}{2}M^2\right) \quad (2)$$

$$\frac{\rho_0}{\rho} = \left(1+\frac{\gamma-1}{2}M^2\right)^{1/(\gamma-1)} \quad (3)$$

$$\frac{P_0}{P} = \left(1+\frac{\gamma-1}{2}M^2\right)^{\gamma/(\gamma-1)} \quad (4)$$

Where A_{ce} = nozzle exit cross-sectional area; A^* = nozzle throat cross-sectional area; T = static temperature at the exit; T_O = total temperature of the primary stream; ρ = static density at the exit; ρ_O = total density of the primary stream; P = static pressure at the exit; P_O = total pressure of the primary stream; M = Mach number; γ = the proportion of specific heat of working fluid. The parameters, including the total pressure of the secondary injection (P_s) and the total temperature of the secondary injection (T_s), are subsequently defined. A corresponding relation for the net force (F) acting is derived in Eq. (5) by employing the one-dimensional isentropic momentum relation concerning sonic jet injection,

$$\sum F = \int \rho V^2 ds = m_s V_s \quad (5)$$

Where m_s = mass flow rate of injected secondary fluid; V_s = average exit velocity. The injected secondary fluid mass flow rate of can be defined as Eq. (6),

$$m_s = P_s M_s A \sqrt{\frac{\gamma}{R_{gc} T_s}} \left(\frac{\gamma-1}{2} M_s^2 + 1\right)^{-\frac{(\gamma-1)}{[2(\gamma+1)]}} \quad (6)$$

Where M_s = Mach number of injected secondary fluid; R_{gc} = gas constant. Through the throat and flap sections of the nozzle, secondary injection is introduced into the primary stream, causing the primary stream and the secondary injection to interact. As a result, the sonic plane skews, deflecting the primary stream and generating a net lateral thrust force in the nozzle. The generated force induces a variation in the pressure distribution across the top and bottom surfaces of the nozzle walls. This investigation involved distinct parameters to estimate the performance of FTS in the modified nozzle configuration. The thrust ratio is defined in the Eq. (7),

$$Thrust\ ratio = F_y/F_x \quad (7)$$

Where the lateral force (F_y), axial force (F_x) and resultant force (F_R) can be calculated by using Eqs. (8), (9), and (10),

$$F_x = mU_{ex} + \int (P_e - P_{amb}) dA_{ex} \quad (8)$$

$$F_y = mU_{ey} + \int (P_e - P_{amb}) dA_{ey} \quad (9)$$

$$F_R = \left(F_x, F_y\right)^T = \int_{A_e} (\rho(w.n)w + (p_e - p_{amb})n) dA \quad (10)$$

$$\delta_\beta = tan^{-1}\left(\frac{F_y}{F_x}\right) \quad (11)$$

Where A_{ex} and A_{ey} = axial and lateral exit cross-sectional area, respectively; U_{ex} and U_{ey} = x and y component of the velocities, respectively; P_e = nozzle area-weighted average exit static pressure; P_{amb} = ambient pressure; δ_β = pitch deflection angle. Furthermore, in previous FTS analyses carried out by Yagle et al. (2001), Deere (2003) and Miller et al. (2012), performance parameters influencing the efficiency and loss of vectored flow along with non-vectored flow in supersonic nozzles drew particular attention. To further evaluate the effects of the FTS injection in the Vikas nozzle upon vectoring performance, three fundamental parameters are employed: the thrust vectoring efficiency (η), the system thrust force ratio ($C_{f,\ g\ sys}$) and the resultant thrust coefficient (K_{TC}).

$$\eta = \frac{|\delta_\beta|}{(m_s/m_p)} \quad (12)$$

$$C_{f,g\ sys} = F_R/(F_{i,p} + F_{i,s}) \quad (13)$$

$$K_{TC} = (\sqrt{F_x^2 + F_y^2})/F_0 \quad (14)$$

Where m_p and m_s = mass flow rate of primary and injected secondary fluid, respectively; F_R = resultant thrust force; $F_{i,p}$ = ideal isentropic nozzle thrust in primary flow; $F_{i,s}$ = ideal isentropic nozzle thrust in secondary injected flow; F_0 = thrust force in non-vectored nozzle.

3. NOZZLE DESIGN MODELLING

Numerous nozzle design models and configurations (Wing et al., 1997; Zmijanovic et al., 2012; Khare & Saha, 2021) were reviewed to perform this investigation effectively; the purpose of design was varied without specialized features and were utilized for more generic applications. Consequently, the bell nozzle is adopted for this research since it offers improved uniform flow distribution, greater flexibility in thrust vectoring angles, and superior efficiency even at lower pressure ratios. The PSLV rockets are frequently used to launch satellites into low earth orbit space; the Vikas engine utilized in the second stage liquid phase from the four compiled stage operations in PSLV is chosen for its effective functioning (Jeyakumar & Biswas, 2003; Guruprasad & Mayilvaganan, 2019).

The PSLV rocket employs the actuating gimballed mechanism in the Vikas engine nozzle to achieve a vectoring angle of ± 4° (Reddy et al., 2021). The nozzle design geometry employed in the current numerical investigation is derived from the previous research work of the contoured divergent Vikas engine nozzle (Shinde & Singh, 2017). Figure 2 illustrates the baseline nozzle design configuration utilized in the numerical investigation. To investigate the thrust vectoring performance of the nozzle and to obtain good aerodynamic

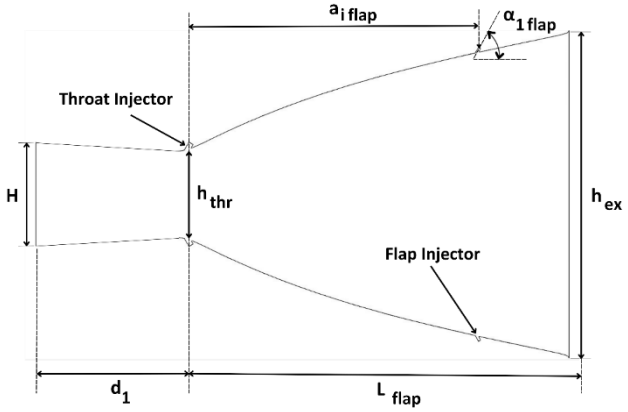

Fig. 2 Baseline configuration of Vikas nozzle

efficiency employing the FTS technique, design parameters for the DOE were obtained from the baseline nozzle illustrated in Fig. 2. The distinct nozzle design configurations stipulated for DOE to assess the design effectiveness of nozzle during vectoring is depicted in Fig. 3. Four distinct design configurations of Vikas nozzle were considered for the DOE approach by varying the design parameters that strongly affected thrust vectoring effectiveness (η). To carry out and perform DOE analysis in a systematic way, various research investigations on the nozzle optimization carried out by Tuttle and Blount (1983); Ali et al. (2012); Yu et al. (2014); Kara & Kurtuluş (2023), were reviewed. These prior research work had specific design variable while maintaining the remaining design parameters as fixed constraints. A similar approach was drawn in this investigation to conduct the DOE analysis. The implemented DOE and Computational Fluid Dynamics (CFD) methodology to acquire an ideal nozzle configuration that is capable of efficient thrust vectoring is stated in Fig. 4. In the phase 2 analysis of nozzle the constant design parameters included contraction ratio (d_1/H) as 1.74 and throat diameter (h_{thr}) as 460 mm. In case of design variables for the phase 2 analysis, the divergent flap length ratio (L_{flap}/h_{thr}) ranged from 1.02 to 4.33; the expansion ratio (A_{ce}/A^*) ratio values for the four nozzles were 4, 6.86, 10.56 and 14.42 respectively; and finally, the nozzle pressure ratio (NPR) was varied according to the nozzle design since the designed chamber pressure for each nozzle was different.

From the phase 2 DOE & CFD analysis of nozzle configurations, the following were inferred,

1. When the divergent flap length was above 3.18 , it results in a lower vectoring effectiveness parameter due to the formation of strong oblique shock waves downstream of the throat injector. This shockwave formation, when intruded with the subsonic turning, the vectoring effectiveness tended to decrease.
2. As the nozzle expansion ratio of nozzles increased from 4 to 14.2, the vectoring effectiveness for each nozzle configurations increased significantly.

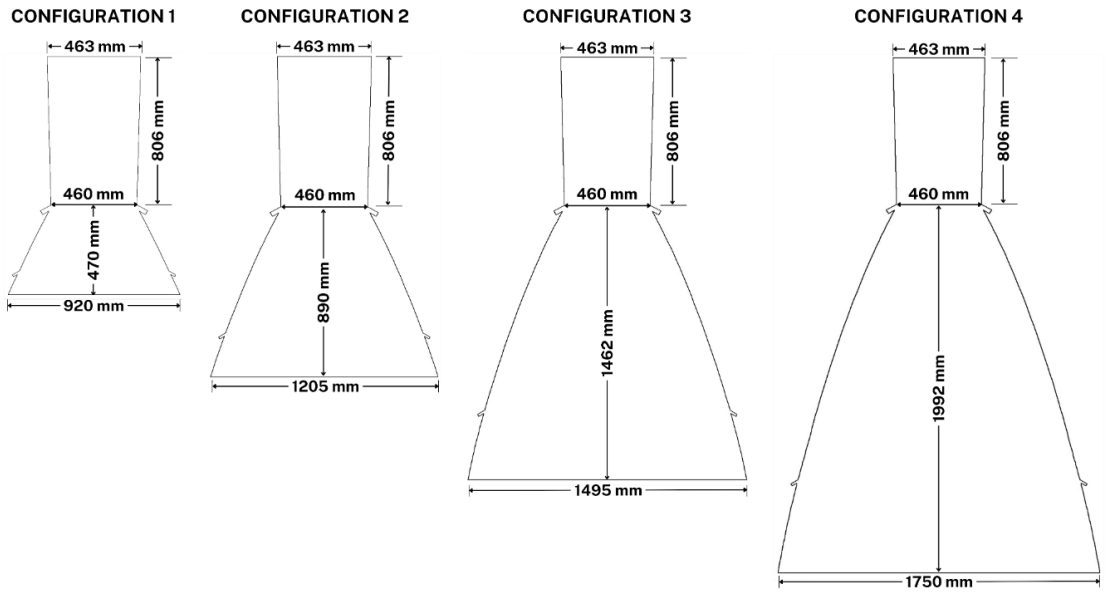

Fig. 3 Design configurations of Vikas nozzle utilized for further DOE investigation

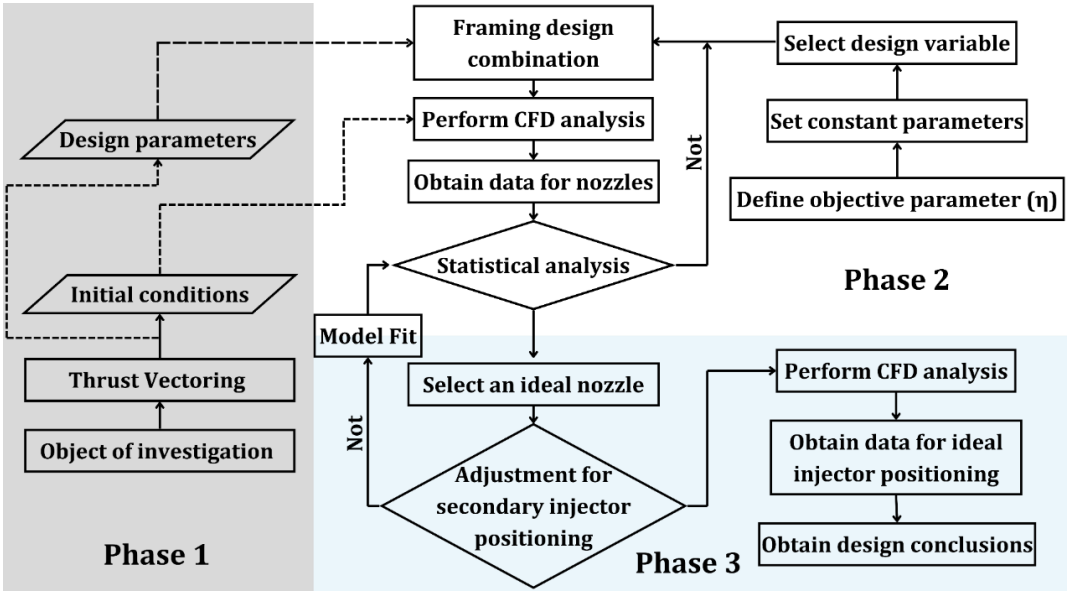

Fig. 4 DOE & CFD investigation methodology process employed to opt an effective nozzle configuration

3. In case of NPR, the vectoring effectiveness showed a slight increase when the NPR is maintained below the designed condition.

With the nozzle design analysis, the nozzle configuration 3 produced optimum results with substantial thrust vectoring effectiveness and hence this design is furthered for the phase 3 analysis. In the phase 3 investigation the prime objective was to identify an ideal injector position for secondary injection. The flap injector location ($a_{i,flap}/L_{flap}$) was considered a design variable with values of 65%, 75% and 85% while the flap injector angle ($\alpha_{i,flap}$) was maintained at a constant value of 60°. From the phase 3 investigation it was inferred that,

1. The length between the throat injector and the flap injector is furthered to determine the degree at which the flow from the throat section can be skewed. Realigning the flap injector in the nozzle aft section can maximize the nozzle length ($a_{i,flap}/L_{flap}$). Hence, the location of flap injector near the nozzle exit tended to increase the vectoring effectiveness.

The numerical results of phase 3 analysis are further discussed in the section 7.3. Therefore, from this investigation, it was evident that divergent flap length, flap injector location, and flap injector angle design factors had a substantial effect on the thrust vectoring with respect to vectoring effectiveness while expansion ratio and contraction ratio had moderate and weak effects respectively in terms of vectoring effectiveness. The investigation conducted by Miller et al. (2012) was utilized to validate the current DOE & CFD analysis. The DOE results are visualized using the CFD results as outlined in Fig. 5.

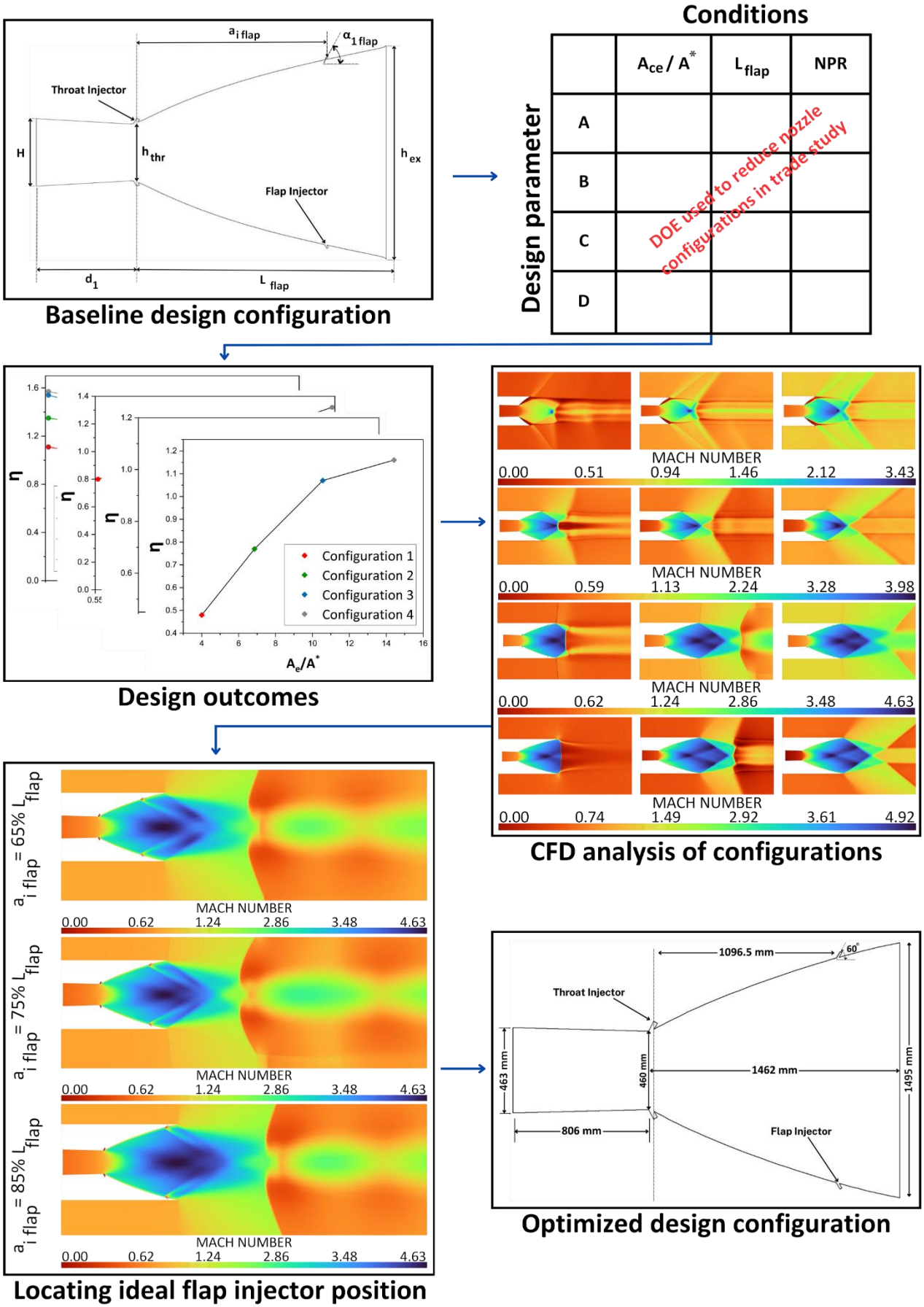

Fig. 5 Infographic depiction of DOE & CFD technique utilized in the investigation to opt an effective nozzle configuration

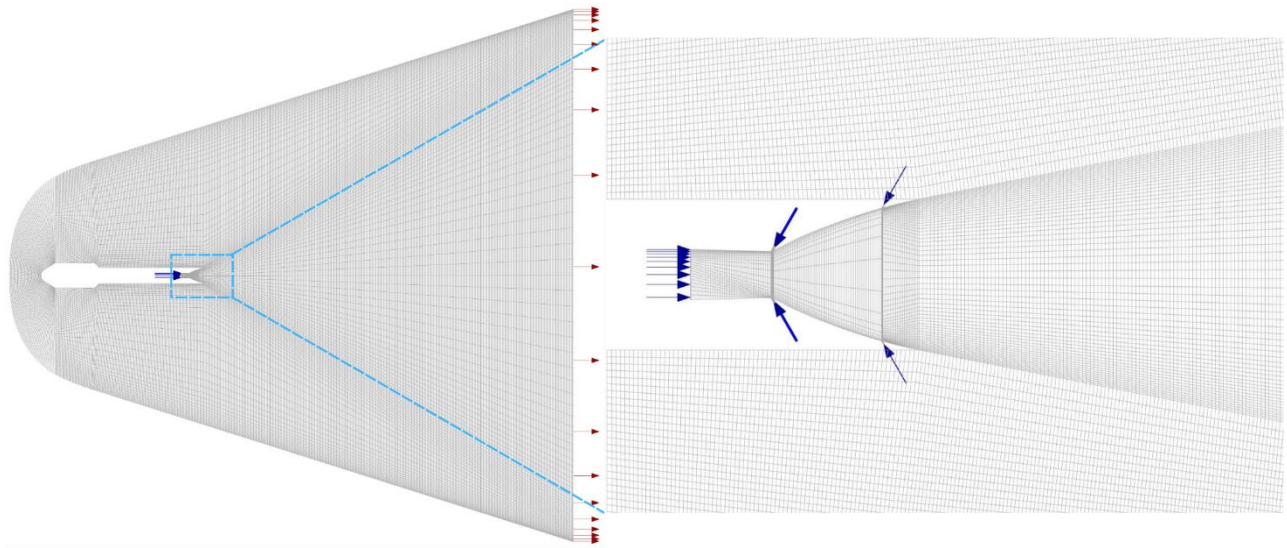

Fig. 6 Flow physics carried out in the nozzle with injector plenums

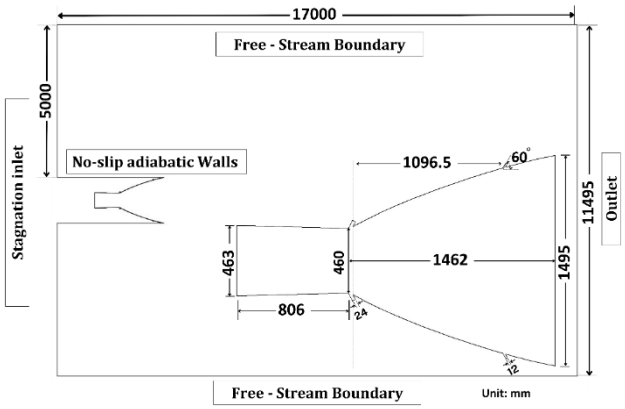

Fig. 7 Computational domain model set with boundaries

4. COMPUTATIONAL DOMAIN

The computational flow physics adopted in Fig. 6 of the designed model establishes the domain boundaries in Fig. 7. For three different Mach conditions, a complete set of simulations is performed. The stagnation inlet is regarded as the main inlet and is operated at distinct NPR at each subsonic, transonic, and supersonic regime. The nozzle performance under dynamic conditions is comprehended by analyzing the optimized nozzle with various NPRs.

The secondary fluid injector plenums used for thrust vectoring are considered the mass flow inlets. The computational analysis is simulated by equally varying the Secondary Mass Flow Rate (SMFR) on the throat and flap sections concerning each iterating Mach condition. The nozzle outer surface is treated as a non-slip and adiabatic wall boundary, and to model the boundary under free-stream conditions, the domain wall is considered the free-stream boundary set with sea-level working conditions. The pressure outlet defines all the exit boundaries. Table 1 summarizes the assumptions used to streamline the intricate computational processes.

Table 1 Numerical Presumptions adopted in analysis

S. No	Descriptions
1	Internal flow field characteristics are kept steady
2	Inlet and outlet section of nozzle are simulated with steady fluid flow parameters
3	Viscous resistance effects are neglected
4	The main inlet is simulated with uniform fluid flow parameters
5	The secondary inlets are simulated with uniform fluid flow parameters

5. MESH SENSITIVITY ANALYSIS

The mesh sensitivity analysis is carried out in this investigation to determine the mesh size meticulously and to increase the accuracy of results. Thus, the analysis is conducted by gradually decreasing the mesh size so that the precision in the result would not vary even if the mesh is discretized further. The static pressure across the nozzle faces for three distinct grid levels is examined in this study to determine the mesh sensitivity by adopting the lowest possible range of element size capable of yielding precise results. The grid convergence indicator (GCI) is utilized to demonstrate the precision and sensitivity level of the mesh in correspondence with the analyses of Wu et al. (2020b) and Zeng et al. (2024). For all three distinct mesh computations, a uniform refinement factor (r) is exhibited across the throat and flap section of the nozzle. Comparative to the sensitivity analysis investigation conducted by Wu et al. (2020a) and Gao et al. (2024), the mesh sensitivity is evaluated under numerical convergence criteria over distinct levels of total nodes in the grid analysis while maintaining the refinement factor and factor of safety (F_S) as constant parameters. The minimal pressure ratio, P_{NW}/P_0, is the grid convergence variable along the lower and upper nozzle wall surface. The minimal pressure ratios for the corresponding sparse mesh (f_S), medium mesh (f_M), and dense mesh (f_D) are 0.21052, 0.17531, and 0.1746,

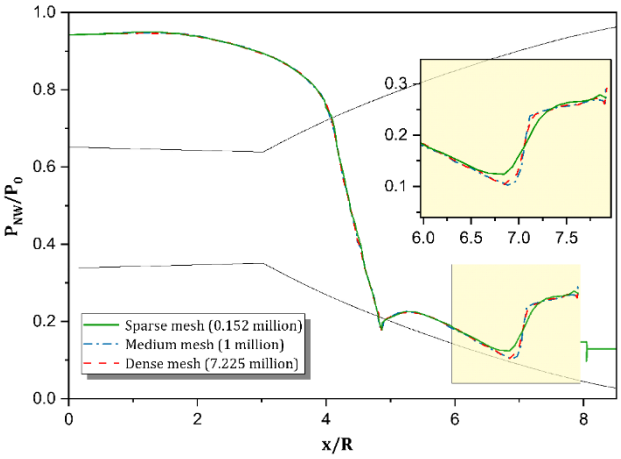

Fig. 8 Mesh sensitive analysis with respect to nozzle wall surface

respectively. The convergence order (j) is estimated from the Eq. (15),

$$j = \ln\left(\frac{f_S - f_M}{f_M - f_D}\right) / \ln(r) = 2.42558002 \quad (15)$$

$$f_{h=0} = f_D + \frac{f_S - f_M}{r^j - 1} = 0.17532461 \quad (16)$$

Where f_S, f_M, and f_D are the minimal pressure ratios for each sparse, medium, and dense mesh level, the Richardson extrapolation is implemented in Eq. (16).

The value of F_s = 1.25 is applied to compute the GCI with the dense mesh resolution. In the case of sparse and medium meshes, the value of GCI is estimated from Eq. (17) and Eq. (18) estimates the GCI value for medium and dense mesh,

$$GCI_{SM} = \frac{F_S \left|\frac{f_M - f_S}{f_M}\right|}{r^j - 1} \text{ x } 100\% = 0.51666448\ \% \quad (17)$$

$$GCI_{MD} = \frac{F_S \left|\frac{f_D - f_M}{f_D}\right|}{r^j - 1} \text{ x } 100\% = 0.01046076\ \% \quad (18)$$

Therefore,

$$\frac{GCI_{SM}}{r^j . GCI_{MD}} = 0.9959003 \approx 1 \quad (19)$$

The determined solution fell closely below the asymptotic interval for convergence, whose value is determined to be almost equivalent to one in Eq. (19).

The three distinct mesh cases are identified corresponding to nozzle wall as depicted in Fig. 8, each with a mesh size of 0.152 million (sparse), 1 million (medium), and 7.225 (dense). The medium and dense mesh static pressure profiles are found to overlap. However, the observations from the static pressure of the sparse mesh differed noticeably from those of both the dense and medium mesh. The accuracy of the consequent solution is determined by several additional factors, including the element's size, type, and level of quality, in addition to the mesh's refinement, transition, and sensitivity. Modifying those parameters that accommodate the model's complexity and output precision was essential. As a result, the mesh model comprising 1 million nodal elements is concluded the best choice for subsequent research and simulations, as it not only assured precision in calculation but also saved computing time. The domain model depicted in Fig. 9 is discretized into smaller nodes using the quad-dominant meshing technique. The quadrilateral nodes are employed to refine the geometry into a structural model since the meshes with quadrilateral nodes are found to provide high accuracy of results for the same density of elements as well as a more straightforward implementation of the desired boundary conditions compared to the meshes with triangular nodes (Yang et al., 2000).

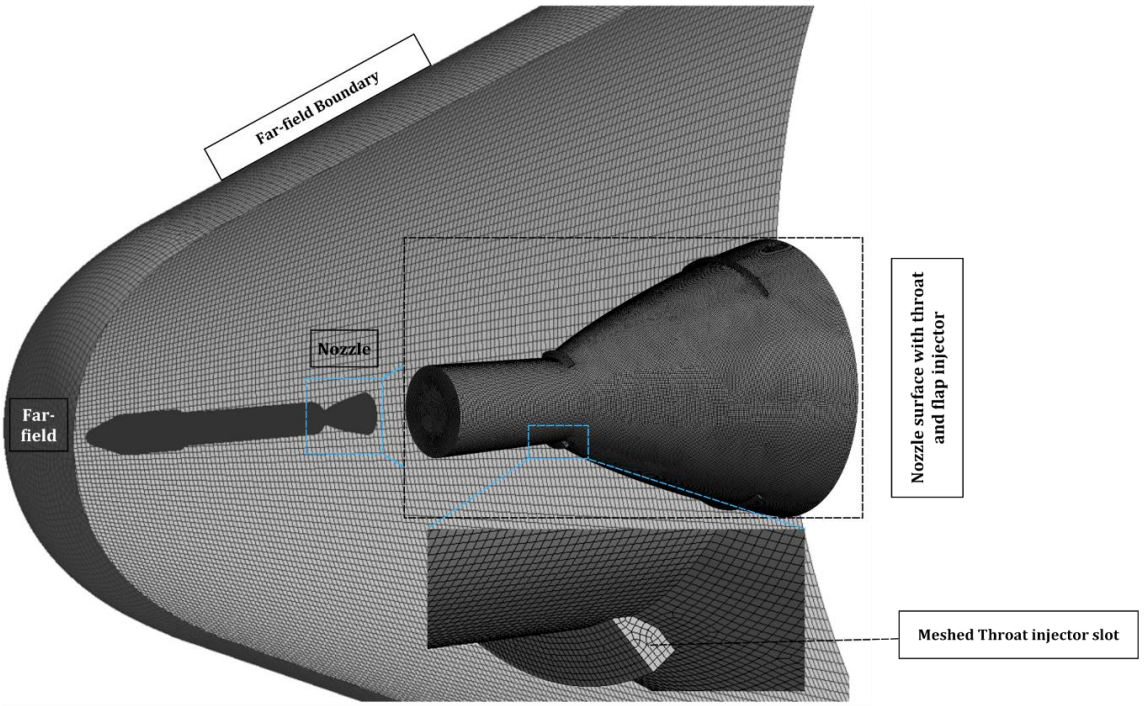

Fig. 9 Mesh of injector plenum within domain field

Table 2 Computational model and boundary conditions

S. No	Numerical parameter	Value assigned
1	Solver type	Density-based solver
2	Working gas	Ideal gas
3	Turbulence model	k-ε realizable model
4	Spatial discretization	Second order upwind
5	Freestream operating mach number (M_∞)	0.6, 0.94, 1.28
6	Freestream pressure (P_{amb})	101325 Pa
7	Stagnation temperature (T_0)	650 K
8	NPR changes Main (pressure) inlet (P_0)	306001.5, 406313.25, 514731, 527903.25, 713328, 723460.5, 928137, 1021356, 1129773.75, 1231098.75, 1321278, 1519875, 2235229.5, 2846219.25 Pa (3.02, 4.01, 5.08, 5.4, 7.04, 7.14, 8.15, 9.16, 10.08, 11.15, 12.15, 13.04, 15, 22.06, 28.09)
9	SMFR changes in throat section Secondary (mass flow) inlet (m_s)	3% - 52 Kg/s; 5% - 86.5 Kg/s; 7% - 121.4 Kg/s; 9% - 156 Kg/s
10	SMFR changes in flap section Secondary (mass flow) inlet (m_s)	3% - 13 Kg/s; 5% - 21.7 Kg/s; 7% - 30.3 Kg/s; 9% - 39 Kg/s

6. MATHEMATICAL MODELING

Mathematical modeling was required to estimate the computational results of the flow field. Ansys Fluent v21.2 was utilized to compute the compressible flows in this analysis. The conservative form of governing equations were chosen for the investigation to enhance the reliability of numerical solutions. Numerical errors and disparities can be reduced by utilizing this model since the flux variables such as continuity, momentum and energy will be treated as dependent variables. The turbulence model for the current investigation was employed based on the testing conducted by Bulat and Bulat (2013) and Cao et al. (2022) which utilized the k-ε realizable model to identify the pressure gradients, aerodynamics, and flow precisely with damping functions implemented on solid wall surfaces to adapt the turbulent viscosity. It was evident that the k-ε yielded better results and provided the boundary layer separation characteristics with superior accuracy, more significant pressure gradients, and more suitable for recirculated and separated flows. The k-ε turbulence model solves two turbulent quantities: the kinetic energy and the dissipation rate. Since this investigation involved the analysis of the secondary flow field, k-ε is preferred. Thus, during the research, the Reynolds-averaged Navier-Stokes (RANS) two-equation k-ε realizable CFD model is employed numerically. A second-order k-ε realizable model provided better precision in obtaining the propagation of jet speed in planar and round jets. A second-order upwind model is employed throughout the spatial discretization process as a high-quality mesh is generated. A coupled method is then used to solve the pressure-velocity coupling because it improves stability and convergence rate. For the controls, explicit relaxation factors with pseudo-time are considered. The dependent variables converged fully when the sum of the residuals was less than 1e-06. Table 2 outlines the crucial boundary conditions and models employed in the computational analysis. The employed transport equations are as follows in Eq. (20) and Eq. (21):

$$\frac{\partial(\rho k)}{\partial t} + \frac{\partial(\rho k u)}{\partial x_i} = \frac{\partial\left[\left(\mu+\frac{\mu_t}{\sigma_k}\right)\frac{\partial k}{\partial x_j}\right]}{\partial x_i} + P_k + P_b + \rho\epsilon - Y_M + S_k \quad (20)$$

$$\frac{\partial(\rho \epsilon)}{\partial t} + \frac{\partial(\rho \epsilon v)}{\partial x_j} = \frac{\partial\left[\left(\mu+\frac{\mu_t}{\sigma_\epsilon}\right)\frac{\partial \epsilon}{\partial x_j}\right]}{\partial x_j} + \rho C_1 S_\epsilon + \rho C_2 \frac{\epsilon^2}{k+\sqrt{\vartheta\epsilon}} + \rho C_1 \epsilon \frac{\epsilon^2}{k} C_{3\epsilon} P_b + S_\epsilon \quad (21)$$

Here, k refers to the kinetic energy, ϵ is the dissipation rate, μ represents the viscosity, μ_t is the molecular turbulent viscosity, σ_k and σ_ε are the turbulent models Prandtl number, P_k and P_b is the shear production term and the buoyancy production term respectively, Y_M is the varying dilation in the compressible turbulence model to the dissipation rate, and C_1, C_2, and C_3 are the empirical constants. S_k and S_ϵ in Eq. (20) and Eq. (21) represent the source terms which are user-defined.

7. RESULT AND DISCUSSION

To obtain the numerical solution of flow field in a precise manner various literature were considered (Carlson & Lee, 1981; Deere, 2003; Miller et al. 2012; Gao et al., 2024; Zeng et al., 2024). From these literatures it was evident that the flow field of a bell nozzle is a crucial factor in obtaining the optimized design and performance; however, it is complex and dynamic, as characterized by its operating regimes. The investigations conducted by Nozzle geometry, operating conditions, and boundary layer effects are the factors that significantly influence the flow field. Considering those parameters, the nozzle is effectively designed to produce high thrust ratios. The computational simulations of the adopted nozzle are obtained regarding Mach number and density contour maps. The NASA LaRC nozzle configuration 2 from the experiment conducted by Carlson and Lee (1981) is employed for the precise numerical result validation of the adopted nozzle configuration utilized in this investigation. The computational data is estimated and correlated with the experimental data of NASA LaRC for

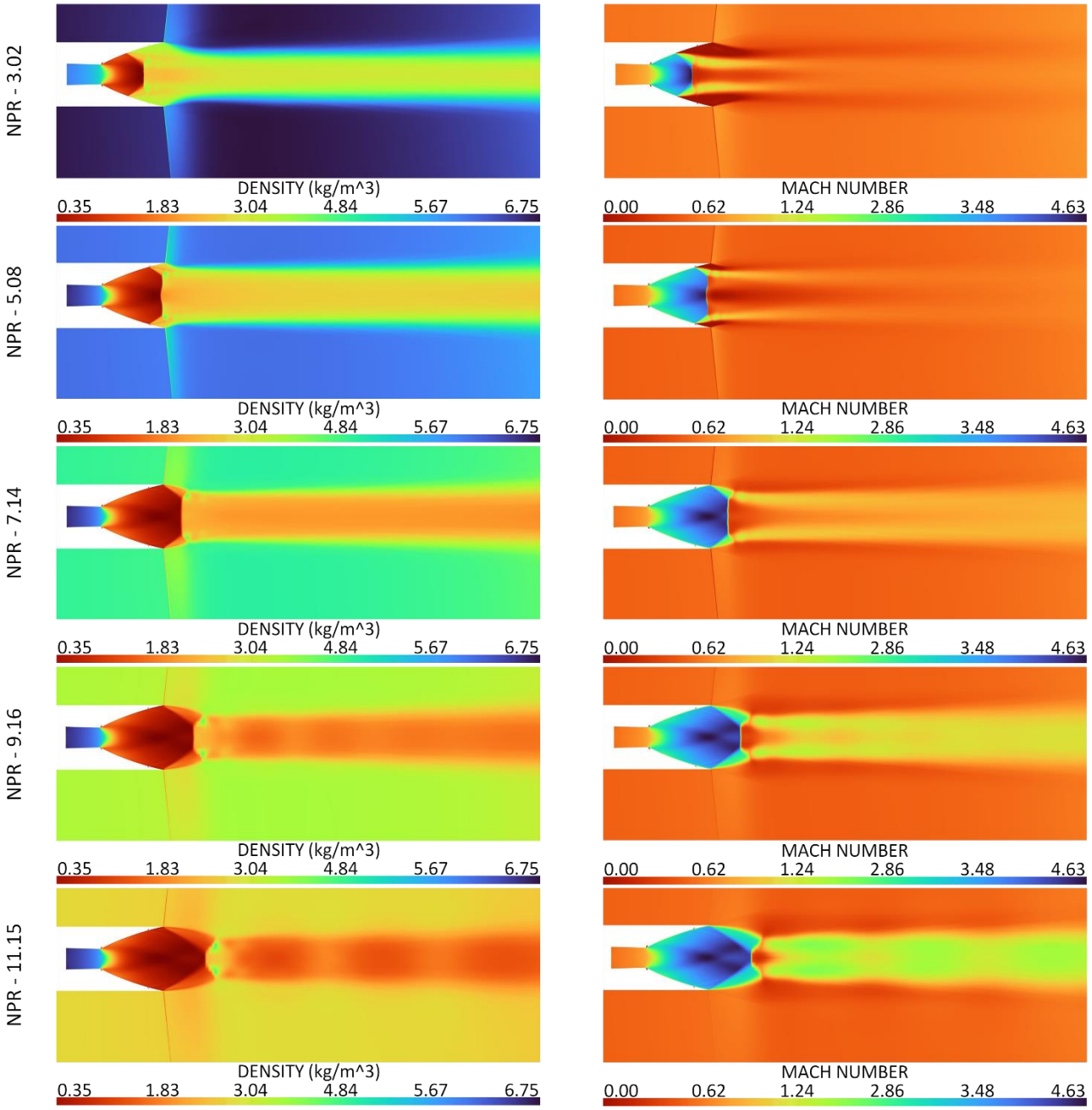

Fig. 10 Density (left) and mach number (right) contour map of nozzle at M_∞ = 0.6 (Subsonic regime)

the corresponding NPR and critical operating Mach (M_∞). In accordance with the experimental NPR parameters, the NPR parameter in the present investigation varied for every critical Mach condition. To assess the nozzle performance, the nozzle configuration 3 is computationally analyzed in three distinct flight conditions encompassed from the subsonic to supersonic speeds, specifically with M_∞ = 0.6, 0.94, and 1.28, without applying the FTS technique.

7.1 Nozzle Performance Analysis in Subsonic, Transonic and Supersonic Regime

The computational analysis of nozzle showed that over-expansion occurs when the nozzle is operated at a lower NPR than the designed NPR condition. As a consequence, Mach disks are formed downstream of the nozzle flow. In Fig. 10, shockwave generation begins once the flow reaches supersonic condition, apparent from NPR 3.02, during which the Mach disk is initially produced. It is observed that with increasing NPR, the Mach disk formation is skewed forward due to the weaker attempt of nozzle flow to expand and match the ambient conditions. Also, while increasing NPR, the wave reflections inside the nozzle flow is visible, and the flow separation region is diminished. At even higher NPR levels, the interference of supersonic shocks and wave reflections is more apparent in the jet stream. The density contours tended to decrease with the increasing NPR, while the Mach contours tended to increase during the expansion and vice versa eventuated throughout the simulation. With the increasing NPR, the pinching effect tended to increase gradually, as observed in Fig. 10. This effect is caused by the difference in adverse pressure gradient developed within the nozzle compared to that of the atmospheric pressure Fig. 10, Fig.

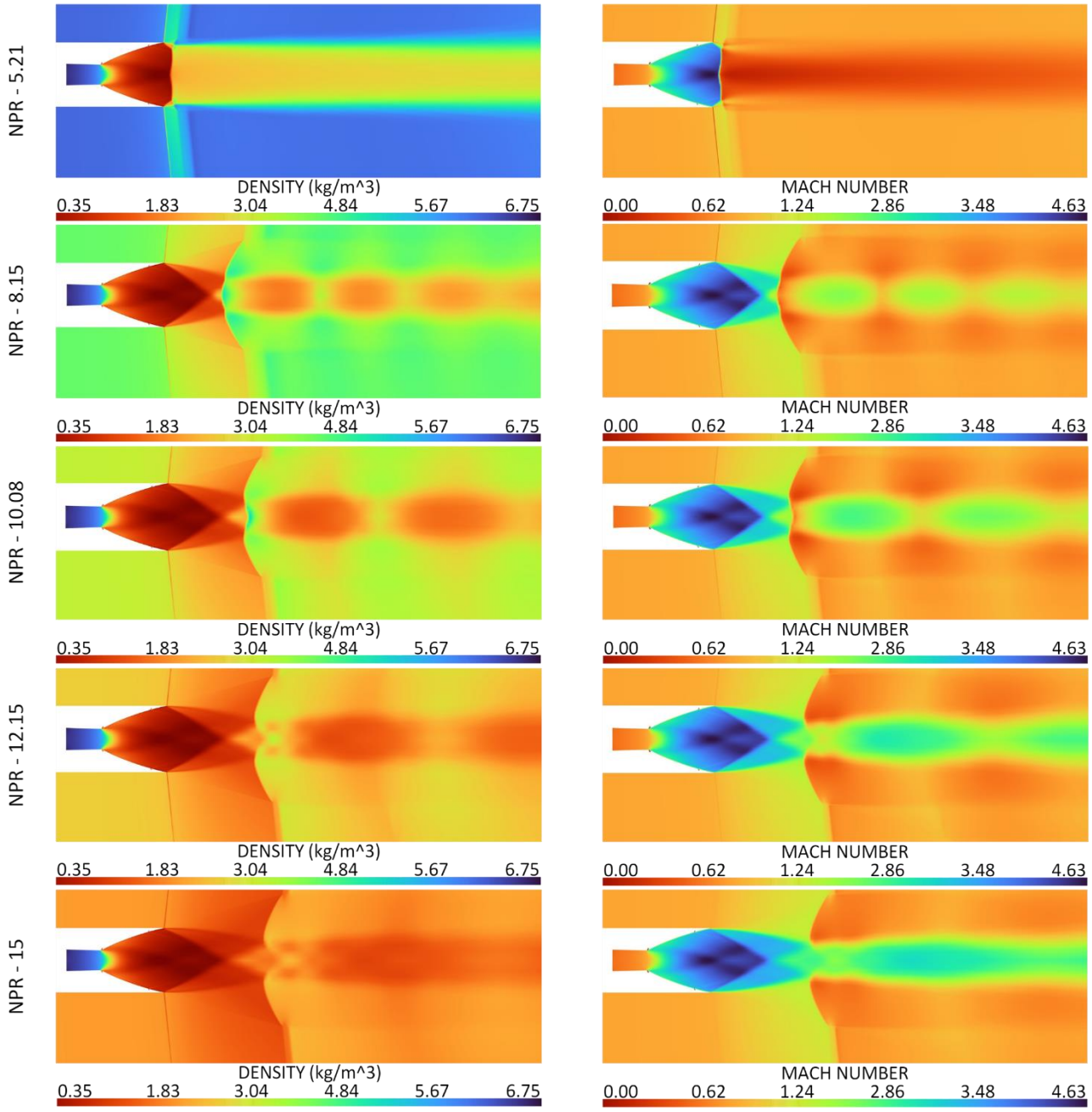

Fig. 11 Density (left) and mach number (right) contour map of nozzle at M_∞ = 0.94 (Transonic regime)

11, and Fig. 12 depict various levels of overexpansion, interference between adjacent flow fields, and adaptation of Mach disk location in the nozzle. Similar variations are observed in density and Mach contour maps of transonic and supersonic flight regimes (Fig. 11 and Fig. 12). Since the divergence angle of the adopted nozzle is maintained the same as the Vikas nozzle, the nozzle walls can contain the overturning of flow. Therefore, the shockwave formation within the nozzle is reduced as the wall pressure gradient, which leaves the throat, decreases. From the computational results, it can be visualized that sufficient resolution of nozzle plumes is attained, and apart from the jet flow, no notable flow perturbations originate from or approach the boundaries. Furthermore, the nozzle domain is unaffected by the interference that the forebody generates. As a result, the sole factors affecting the jet stream emanating through the nozzle are the external pressure and the overall flow state in the boattail section.

7.2 Numerical Validation with Experimental Data

The experimental investigation of Carlson and Lee (1981) in NASA LaRC was conducted in a transonic wind tunnel section with five distinct nozzle configurations. The experiment involved the investigation of internal and external pressure distribution of nozzle along with static thrust co-efficient. Each nozzle configurations were tested at increasing NPR for six distinct operating mach. The adopted nozzle configuration results are correlated with the experimental data's values since each case's separation point is accurately estimated. The results of this investigation are compared with the experimental data across three different Mach operating regimes to evaluate the accuracy of the computational results. The finest

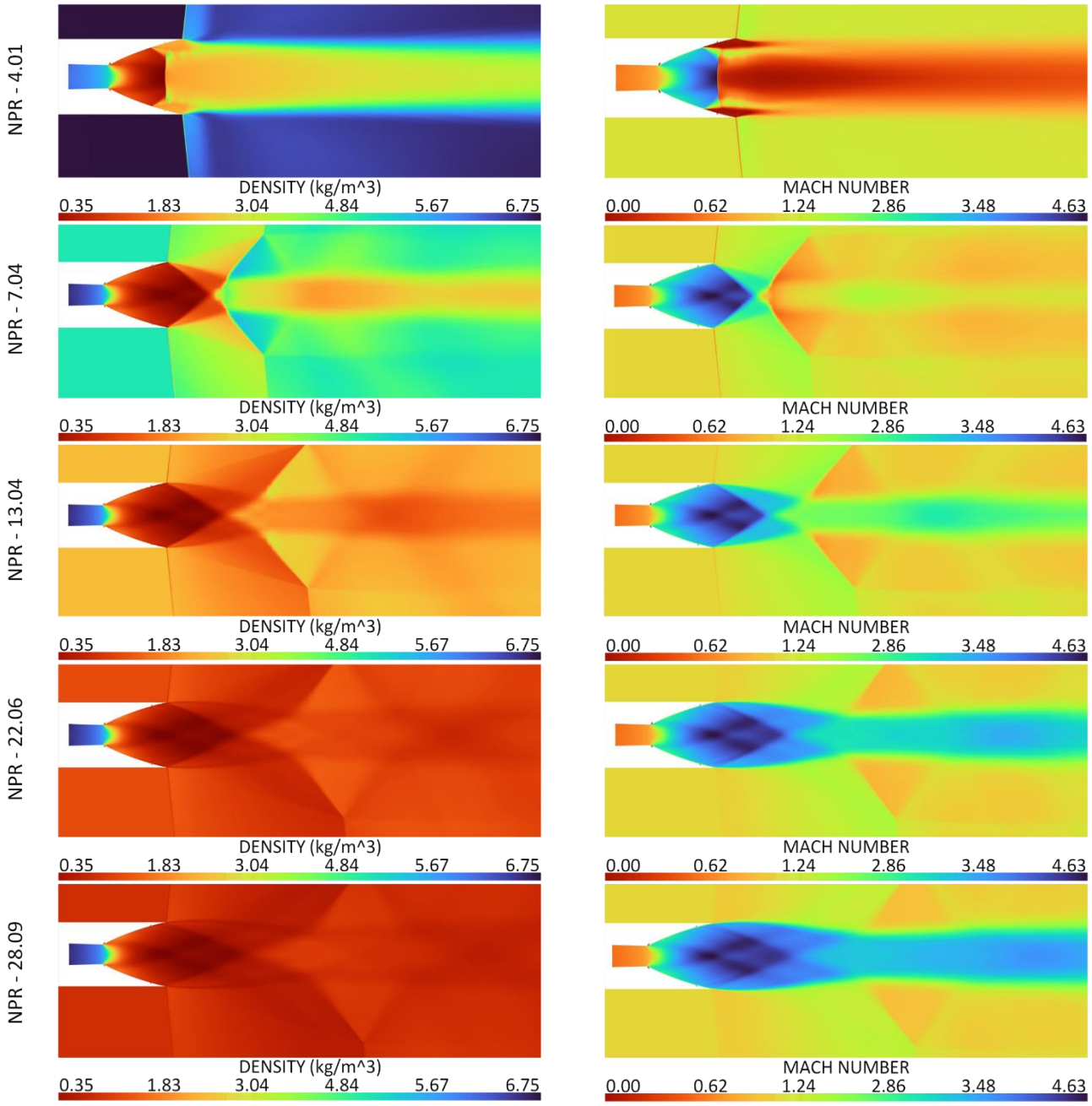

Fig. 12 Density (left) and mach number (right) contour map of nozzle at M_∞ = 1.28 (Supersonic regime)

results are achieved with a higher NPR, notably for NPR > 3.02. The graphical plot representing the comparison of computational results with the accessible experimental data values for the nozzle's internal and external pressure distribution is depicted in Fig. 13, Fig. 14, and Fig. 15 respectively. The distribution of internal pressure within the nozzle is independent of the external environment until the exit jet stream reached supersonic speed. The distribution of internal pressure within the nozzle is independent of the external environment until the exit jet stream reached supersonic speed. Increasing M_∞ in the freestream led to a diminished internal pressure distribution throughout the flow-separated zone. The internal nozzle pressure distribution of the nozzle attempted to skew the separation further downstream, as seen in Fig. 13. Furthermore, M_∞ increased from 0.94 to 1.28 in Fig. 14, and Fig. 15 the external flow experienced in the transonic and supersonic expansion across the nozzle exit, significantly reducing pressure. The nozzle internal pressure distribution exhibited shock-induced flow across the diverging section, with the NPR significantly lower than the designed NPR. Therefore, at lower NPRs, it is adequate to predict that it will cause the drag and overexpansion associated with the diverging section of the nozzle to increase. A minimum NPR > 7 is necessary to prevent flow separation in the adopted nozzle configuration. Evidently, the flow separation traveled towards the exit and vanished as NPR increased with increasing total jet pressure. The external pressure showed that as P_{jt}/P_∞ increased, the external nozzle flow separation occurred downstream, and the shockwave in the nozzle's trailing edge tended to move upstream. Consequently, the jet interference in the external flow stream caused immense effects. Figure 13(b) depicts that the surface pressure of the boattail tended to decrease as

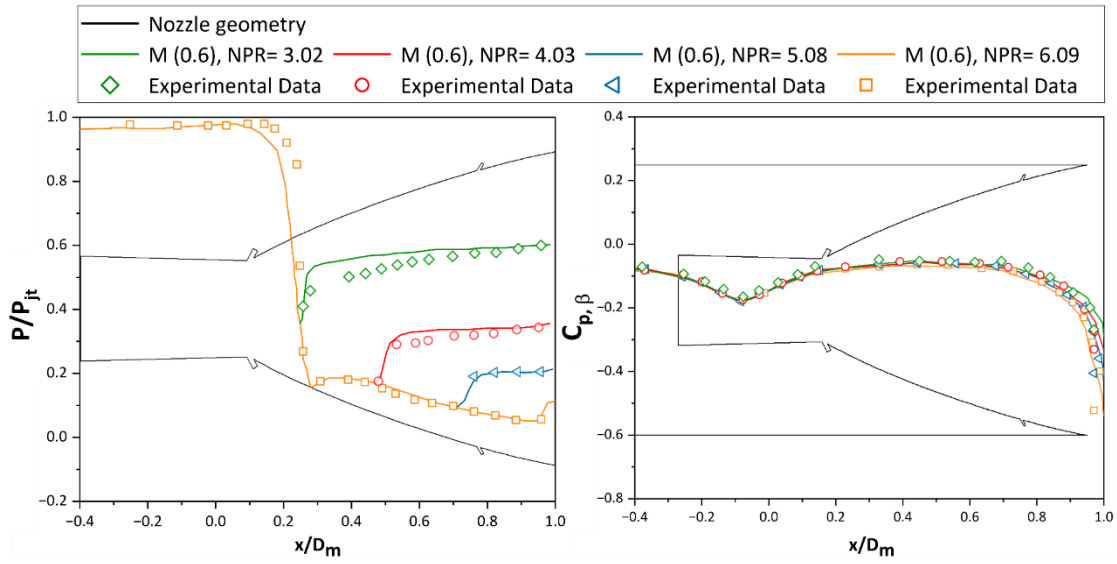

(a) (b)

Fig. 13 Experimental & adopted nozzle a) internal and b) external pressure distribution at subsonic speed

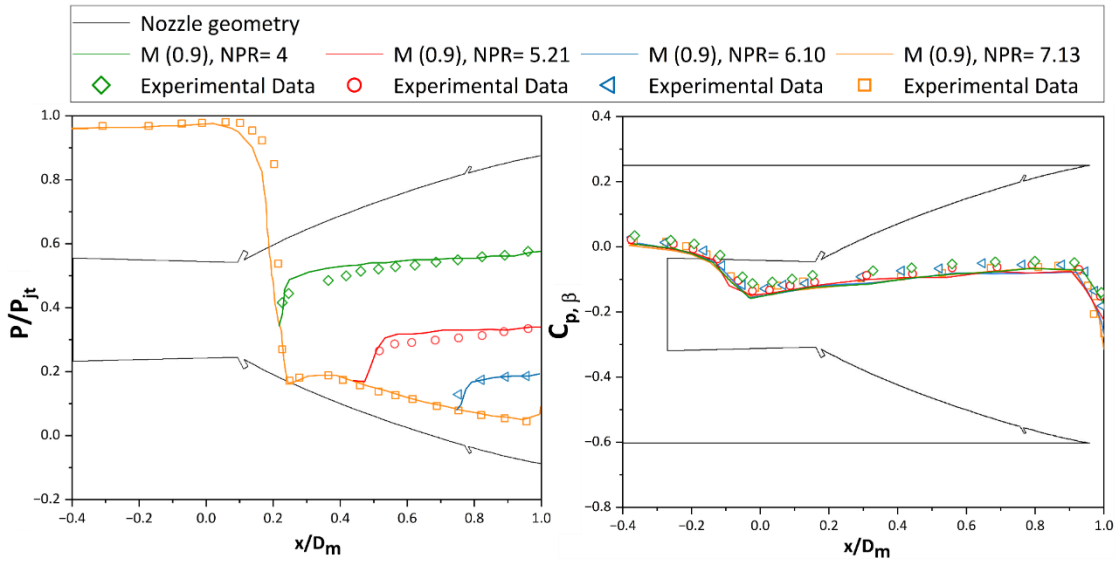

(a) (b)

Fig. 14 Experimental & adopted nozzle a) internal and b) external pressure distribution at transonic speed

P_{jt}/P_{∞} increased, signifying adverse jet effects. Since downstream interference can only propagate forward across the subsonic region, the jet operation tends to have minimal or almost no impact on the external pressure distribution of the boattail forward section at supersonic speeds (Fig. 14(b)). At supersonic Mach regimes (Fig. 15 (b)), the nozzle expansion across the rear portion of the boattail progressively concentrates towards an expansion fan located downstream, confining the nozzle pressure distribution. For the given distinct critical Mach conditions and operating NPR of the nozzle, the overall CFD results for internal and external pressure distribution are in good agreement with the NASA LaRC experimental results. Therefore, these understandings were utilized to investigate the FTS effects in the nozzle configuration 3.

7.3 FTS Vectoring

To facilitate the computational analysis of the adopted nozzle configuration, the flap injector is progressively positioned at 65%, 75%, and 85% of the total diverging length of the nozzle. The analysis is performed until the precise positioning of the formed fluidic ramp in the nozzle is established sufficiently for efficient vectoring. Figure 16 represents the positioning of flap injectors at different diverging lengths of the nozzle. The injector plenum in the throat and flap section of the nozzle is placed normal to the nozzle wall at 60° to attain optimum thrust vectoring deflection. The throat injector plenum skewed the position of the sonic plane nearer to the flap by expanding the restricted flow area closer to the injector plenum. When the injector plenum position is too distant

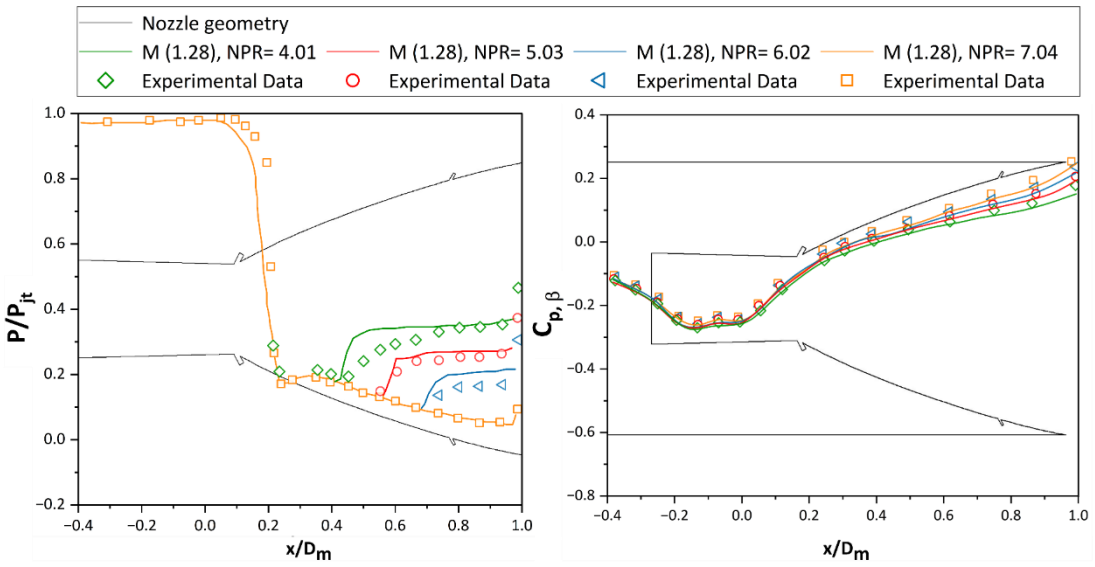

(a) (b)

Fig. 15 Experimental & adopted nozzle a) internal and b) external pressure distribution at supersonic speed

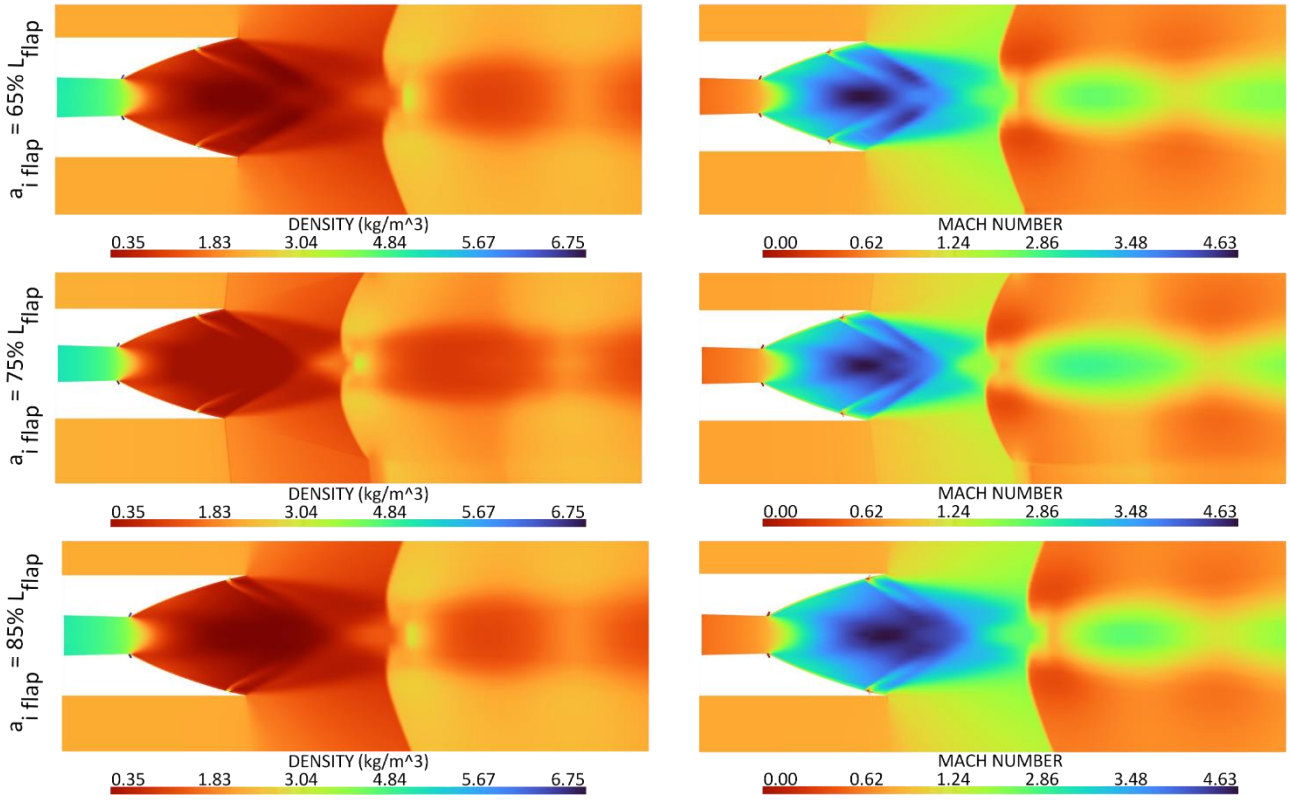

Fig. 16 Density (left) and mach number (right) contour map for distinct diverging flap locations ($a_{i,flap}/L_{flap}$) of nozzle configuration 3

upstream, the flow separation is not effectual, and reattachment of flow is observed for that amount of mass flow rate per unit area. Nevertheless, such difficulty is rectified when either the injector plenum area size is limited, the mass flow rate per unit area is increased, or with the aid of both cases. With these constraints, the resolution is made by positioning the slot at 75% of the divergent flap length, which is considered adequate for the subsequent vectoring analysis. The critical Mach condition (M_∞ = 0.94), the nozzle pressure (NPR = 10.08), and an equal amount of SMFR in the throat and flap section are maintained in the nozzle setup throughout this section to expedite the effective fluidic throat skewing vectoring study. The SMFR range is varied from 3% to 9%. In the preliminary investigation (Fig. 16) to determine the optimum positioning of the injector, the SMFR in the throat and flap section is retained at a rate of 2% of the primary mass flow. The investigation showed that

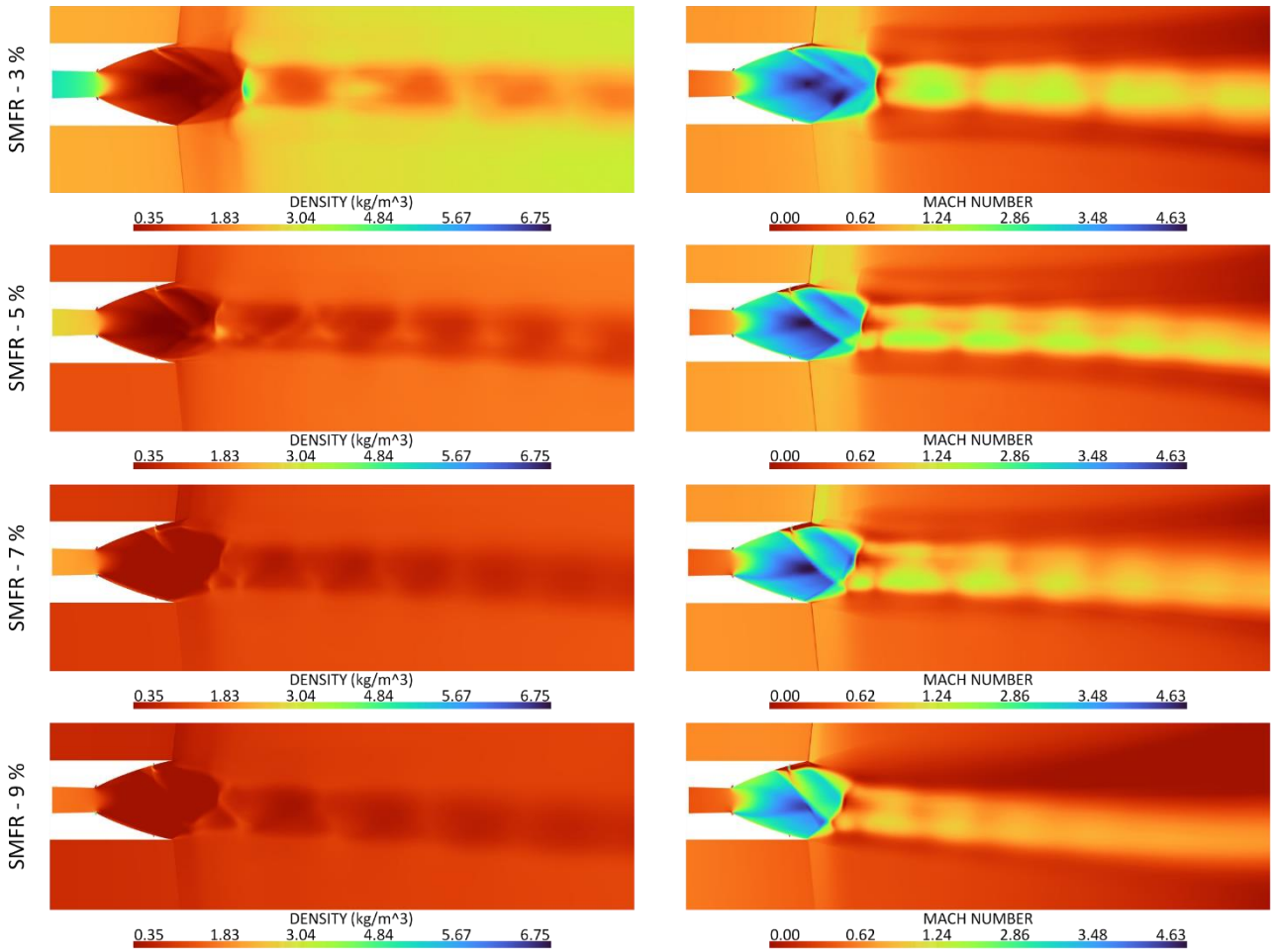

Fig. 17 Density (left) and mach number (right) contour map of adopted nozzle for downward FTS deflection

injecting secondary fluid at an equal mass flow rate in a smaller area is substantially more than the resulting mass flux. As a result of the secondary fluidic injection, the asymmetric pressure loading on the nozzle section caused the primary flow to produce a deflection in the direction concerning the applied SMFR. The primary flow is sub-sonically deflected downward when the secondary fluid injection occurs through the throat injector – 2 and flap injector – 1. Figure 17 depicts the fluidic thrust vectoring of the adopted nozzle with an increasing range of SMFR in throat injector – 2 and flap injector – 1. Similarly, the primary flow is sub-sonically skewed upward when the secondary fluid injection occurs through the throat injector – 1 and flap injector – 2. Figure 18 illustrates the formation of primary flow fluidic ramps caused by increasing SMFR in the throat injector – 1 and flap injector – 2.

7.4FTS Vectoring Effects on Nozzle Performance Parameters

The FTS skewing had significant effects on the nozzle performance parameters. With increasing SMFR, the thrust vector angle is observed to increase. At SMFR – 7% and SMFR – 9%, the shifting of the sonic plane is visible. Additionally, the axial force component tended to decrease as the SMFR increased. In actual cases, the asymmetric pressure gradient in the nozzle and the resulting primary flow deflection would likely be produced devoid of entirely skewing sonic plane location. Figure 19 represents the deflection attained by the nozzle for the respective SMFR. With the introduction of injected secondary fluid mass flow rate (m_s) to the primary flow, the δ_β tended to increase. Since flow chocking entirely occurred in the newly skewed aerodynamic minimum cross-sectional area, the nozzle pitch deflection is performed effectively. The asymmetric pressure difference induced in the nozzle due to subsonic deflection caused a rapid increase in F_y, which, as a result, improved K_{TC}, as shown in Fig. 20 (a). The direct relation between η and SMFR is also expressed in Fig. 20 (a). When the injector plenum is supplied with SMFR = 3%, maximum η is attained. Although δ_β increased with increasing SMFR, η is reduced through throat skewing due to the escalation of the injected secondary fluid mass flow rate (m_s). The contoured Vikas nozzle configuration 3 produced an estimated axial force of 535.5745 kN in the non-vectored flow. The axial force exerted for SMFR = 9% is reduced by 0.21% compared to non-vectored flow. While performing the FTS vectoring, increasing SMFR raised the F_y component consequentially with an average of 9.04 kN. When the secondary air is introduced to produce deflection, the nozzle induces a total lateral force of 46.7603 kN in the corresponding primary flow. As a result, in the vectored flow, the total axial force produced in the nozzle tended to decrease by 0.17%. Figure 20 (b) represents the system thrust force

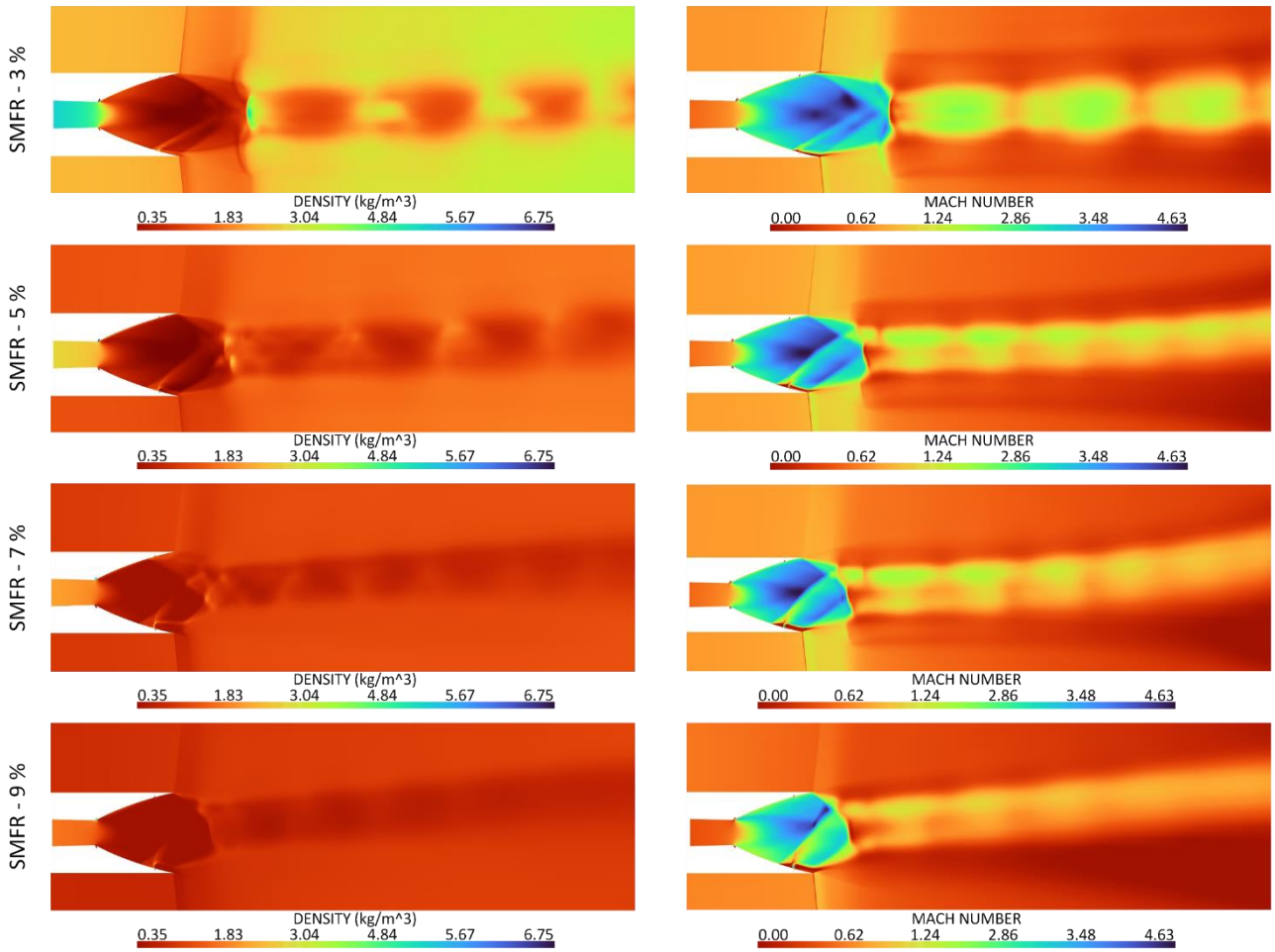

Fig. 18 Density (left) and mach number (right) contour map of adopted nozzle for upward FTS deflection

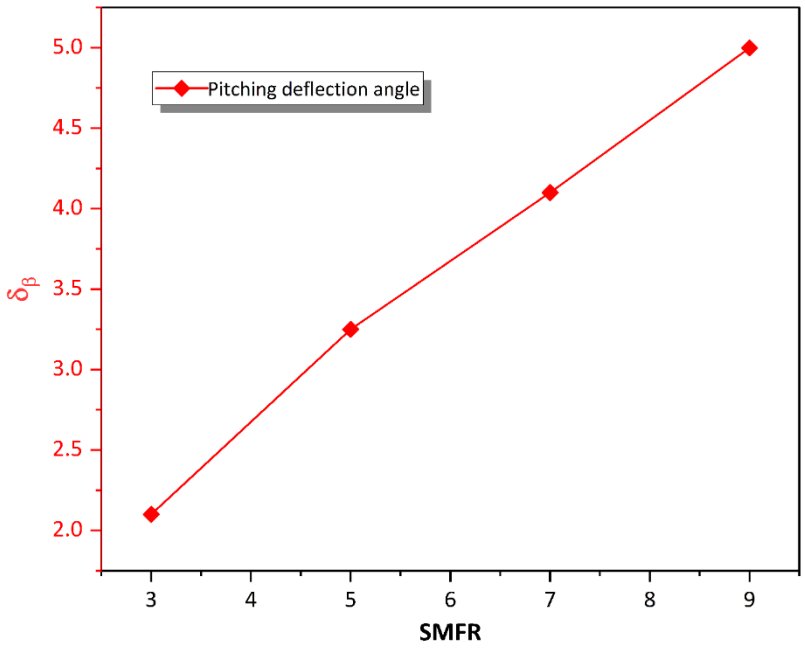

Fig. 19 Deflection angle produced for the corresponding SMFR

ratio and thrust ratio as a function of SMFR. It is inferred that flow separation is caused by introducing a new sonic plane and an increase in F_y due to the secondary fluid injection at the throat and flap section. Since SMFR gradually increased, the separation zone grew without affecting the F_x component, as only a negligible variation is produced in the F_x component. The linear regression of $C_{f,\,g\,sys}$ is depicted in Fig. 20 (b) Compared with the non-vectored condition, when the SMFR is maintained at 3% $C_{f,\,g\,sys}$ is decreased to 2.88%, and when SMFR is increased to 9% $C_{f,\,g\,sys}$ is further decreased to 8.09%. This decrease in $C_{f,\,g\,sys}$ is caused due to the flow separation occurring in

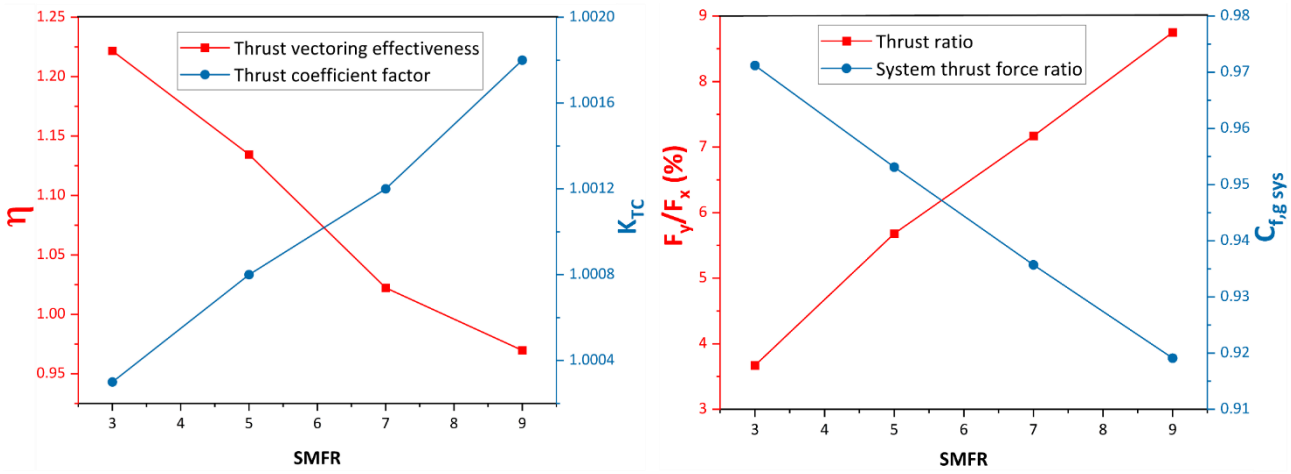

(a) (b)

Fig. 20 Effect of secondary fluid injection on a) thrust vectoring effectiveness and thrust co-efficient b) thrust ratio and system thrust force ratio

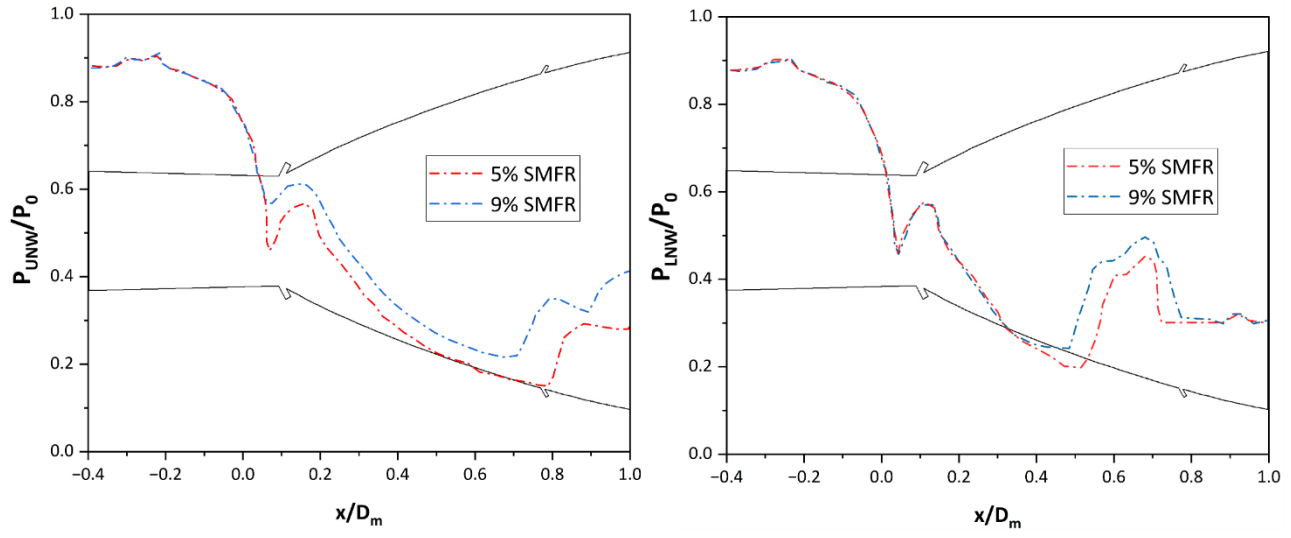

(a) (b)

Fig. 21 Effect of secondary fluid injection on total pressure for NPR = 10.08 with M_∞ = 0.94 freestream condition a) upper wall b) lower wall

the nozzle walls. An average decrement of 2% is exhibited in $C_{f,\,g\,sys}$ when the SMFR is ranged from 3% to 9%. Figure 21 illustrates the total internal wall pressure variation between 5% and 9% SMFR computed to assess the nozzle effectiveness on FTS operation.

It is inferred that the total pressure produced in 9% of secondary injections is higher than that produced in 5% of secondary injections; the difference in total pressure results from increased asymmetric pressure loading on the nozzle walls.

8. CONCLUSION

In this computational investigation, a contoured Vikas nozzle was utilized as a baseline design configuration for the design of experiments approach and was then iterated with four distinct design configurations to identify an enhanced and effective nozzle design that can be incorporated with the FTS thrust vectoring control. Specific nozzle design parameters for the design analysis were varied in each configuration. The nozzle configuration 3 was adopted as an optimum nozzle with moderate divergent flap length. The internal and external performance analysis of the adopted nozzle was performed under subsonic (0.6), transonic (0.94), and supersonic (1.28) freestream Mach conditions. With increasing NPR, the nozzle experienced overexpansion, and significant wave interference was apparent with the adjacent surfaces. The high-fidelity nozzle flow characteristics derived from the computational solutions were appropriately validated with the availability of experimental data concerning internal-external pressure distribution. The comparison of both results signified that, with corresponding NPR and freestream Mach, the

computational results and experimental results tended to coincide. The internal pressure distribution of the nozzle was significantly reduced with increasing freestream mach. With increasing jet pressure, the external pressure distribution of the nozzle decreased, indicating adverse effects on the jet stream. At distinct divergent flap injector locations, the nozzle response to secondary fluid was estimated, and the divergent flap injector located at 75% was furthered to proceed with the computational simulation. The FTS vectoring analysis was performed with freestream mach = 0.94, NPR = 10.08, and by progressively varying SMFR up to 9%. With a relatively small amount of thrust losses in the axial direction, the investigation results indicated that an asymmetrical pressure loading in the lateral direction caused crucial subsonic turning of the primary flow. The nozzle performance parameters, namely, thrust vectoring efficiency and system thrust force ratio, were estimated to reduce up to 20.63% and 5.36%, respectively. In comparison, the resultant thrust coefficient increased to 0.14% from the initial condition with the increasing SMFR.

ACKNOWLEDGEMENTS

The computational systems in central research facilities of Bannari Amman Institute of Technology are utilized by the authors to effectively complete the designing and numerical analysis involved in this research, for which we are very grateful to the institute.

CONFLICT OF INTEREST

The authors have no conflicts and are interested to publish this paper in JAFM.

AUTHORS CONTRIBUTION

Thangavelu Harish Ragavendra, **Parangottil Ajidkumar Anupama** and **Kandasamy Sundaram Jai Pranesh** contributed their work in domain research, model designing, computational analysis of the model and article documentation. **Dhanamani Lakshmanan** and **Ramanathan Abinaya**: contributed their work by providing technical assistance and opinions on the paper.

DATA AVAILABILITY

The data that support the findings of the investigation are available from corresponding author upon a reasonable request.

REFERENCES

Afridi, S., Khan, T. A., Shah, S. I. A., Shams, T. A., Mohiuddin, K., & Kukulka, D. J. (2023). Techniques of fluidic thrust vectoring in jet engine nozzles: A review. *Energies, 16* (15), 5721. https://doi.org/10.3390/en16155721.

Ali, A., Rodriguez, C. G., Neely, A. J., & Young, J. (2012). *Combination of fluidic thrust modulation and vectoring in a 2D nozzle.* 48th AIAA/ASME/SAE/ASEE Joint Propulsion Conference & Exhibit. https://doi.org/10.2514/6.2012-3780.

Anderson, J. D. (2004). *Modern compressible flow: Quasi-one-dimensional flow*. Boston McGraw-Hill.

Banazadeh, A., & Saghafi, F. (2017). An investigation of empirical formulation and design optimization of co-flow fluidic thrust vectoring nozzles. *The Aeronautical Journal, 121* (1236), 213-236. https://doi:10.1017/aer.2016.110.

Bulat, M. P., & Bulat, P. V. (2013). Comparison of turbulence models in the calculation of supersonic separated flows. *World Applied Sciences Journal, 27* (10), 1263-1266. https://10.5829//idosi.wasj.2013.27.10.13715.

Cao, Q., Lui, M., Li, X., Lin, C. H., Wei, D., Ji, S., Zhang, T., & Chen, Q. (2022). Influencing factors in the simulation of airflow and particle transportation in aircraft cabins by CFD. *Building and Environment. 207*. https://doi.org/10.1016/j.buildenv.2021.108413.

Carlson, G. T., & Lee, E. E. (1981). *Experimental and analytical investigation of axisymmetric supersonic cruise nozzle geometry at mach numbers from 0.6 to 1.3.* NASA-TP-1953 L-14661.

Chen, J. L., & Liao, Y. H. (2020). Parametric study on thrust vectoring with secondary injection in a convergent divergent nozzle. *Journal of Aerospace Engineering. 33* (4). https://doi.org/10.1061/(ASCE)AS.1943-5525.0001136.

Deere, K. A. (2003). *Summary of fluidic thrust vectoring research conducted at NASA Langley research centre. The 21* AIAA Applied Aerodynamics Conference. 23681.

Deng, R. Y., Kong, F. S., & Kim, H. D. (2014). Numerical simulation of fluidic thrust vectoring in an axisymmetric supersonic nozzle. *Journal Mechanical Science and Technology 28*(12), 4979–4987. https://doi.org/10.1007/s12206-0141119-x.

Faheem, M., Khan, A., Kumar, R., Khan, S. A., Asrar, W., & Sapardi, A. M. (2021). Experimental study on the mean flow characteristics of a supersonic multiple jet configuration. *Aerospace Science and Technology, 108*, 106377. https://doi.org/10.1016/j.ast.2020.106377.

Ferlauto, M., & Marsilio, R. (2017). Numerical investigation of the dynamic characteristics of a dual throat-nozzle for fluidic thrust-vectoring. *AIAAJ. 55* (1). https://doi.org/10.2514/1.J055044.

Flamm, J. D. (1998). *Experimental study of a nozzle using fluidic counterflow for thrust vectoring.* 34th AIAA/ASME/SAE/ASEE Joint Propulsion Conference and Exhibit. https://doi.org/10.2514/6.1998-3255.

Forghany, F., Rahni, M. T., & Ghohieh, A. A. (2017). Numerical investigation of optimization of injection

angle effects on fluidic thrust vectoring. *Journal of Applied Fluid Mechanics*. *10*(1), 157. https://doi.org/10.18869/acadpub.jafm.73.238.26519

Forghany, F., Rahni, M. T., & Ghohieh, A. A. (2018). Optimization of freestream flow effects on thrust shock vector control nozzle. *Journal Applied Fluid Mechanics*, *11*(2), 361-374. https://10.29252/jafm.11.02.28243.

Gao, J., Yuan, Z., Hou, Y., & Chen, W. (2024). Numerical study on the influence of plugging rate on the performance of adjustable steam ejector. *International Journal of Fluid Engineering*, *1*(2). https://doi.org/10.1063/5.0204421.

Guruprasad, B. R., & Mayilvaganan, M. (2019). PSLV: the versatile workhouse launch vehicle of india. *Journal of Aerospace Science and Technologies*, *71*(1). http://dx.doi.org/10.61653/joast.v71i1.2019.112.

Hamid, K. S. A. (1989). *Three-dimensional calculations for underexpanded and overexpanded supersonic jet flows.* 7th Applied Aerodynamics Conference. https://doi.org/10.2514/6.1989-2196.

Ikaza, D. (2000). *Thrust vectoring nozzle for modern military aircraft.* Active Control Technology for Enhanced Performance Operational Capabilities of Military Aircraft, Land Vehicles and Sea Vehicles. 11.1–11.10.

Isaac, J. J., & Rajashekar, C. (2014). Fluidic thrust vectoring nozzles. *Semantic Scholar*. https://api.semanticscholar.org/CorpusID:114481763

Jankovic, A., Chaudhary, G., & Goia, F. (2021). Designing the design of experiments (DOE) – An investigation on the influence of different factorial designs on the characterization of complex systems. *Energy and Buildings*, *250*, 111298. https://doi.org/10.1016/j.enbuild.2021.111298.

Jeyakumar, D., & Biswas, K. K. (2003). Stage separation system design and dynamic analysis of ISRO launch vehicles. *Journal Aerospace Sciences and Technologies*, *55*(3), 211–222. https://doi.org/10.61653/joast.v55i3.2003.761.

Jingwei, S. H. I., Zhanxue, W. A. N. G., Li, Z. H. O. U., & Xiaolin, S. U. N. (2018). Investigation of flow characteristics of SVC nozzles. *Journal of Applied Fluid Mechanics* *11*(2), 331-342. https://doi.org/10.29252/jafm.11.02.28294

Jingwei, S., Zhanxue, W., Li, Z., & Xiaolin, S. (2020). Investigation on flow characteristics and performance estimation of a hybrid SVC nozzle. *Journal of Applied Fluid Mechanics* *13*(1), 25-38. https://doi.org/10.29252/jafm.13.01.29804

Kara, E., & Kurtuluş, D. F. (2023). Determination of optimum parameter space of a fluidic thrust vectoring system based on system based on coanda effect using gradient-based optimization technique. *Journal of Applied Fluid Mechanics* *16*(10), 1974-1988. https://doi.org/10.47176/jafm.16.10.1855

Khare, S., & Saha, U. K. (2021). Rocket nozzles: 75 years of research and development. *Sādhanā, 46*, 76. https://doi.org/10.1007/s12046-021-01584-6

Lai, G., & Sheng, W. (2023). Supersonic reacting jet flows from a three-dimensional divergent conical nozzle. *Society of Industrial and Applied Science*, *55*(5). https://doi.org/10.1137/22M1529099.

Li, L., & Saito, T. (2012). Numerical and experimental investigations of fluidic thrust vectoring mechanism. *International Journal Aerospace Innovations*, *4*(1), 53-64. https://doi.org/10.1260/1757-2258.4.1-2.53

Li, Q., Yao, H., Chen, J., & Luo, X. (2024). Bypass pigging technology in improving pigging safety and efficiency: Principles, progress, and potentials. *International Journal of Fluid Engineering*, *1*(2), 020602. https://doi.org/10.1063/5.0202414

Lim, C. M., Kim, H. D., & Setoguchi, T. (2006). *Studies on thrust vector control using a fluidic counter-flow concept.* 42nd AIAA/ASME/SAE/ASEE Joint Propulsion Conference & Exhibit. https://doi.org/10.2514/6.2006-5204.

Miller, D. N., Yagle, P. J. & Hamstra, J. W. (2012). *Fluidic throat skewing for thrust vectoring in fixed geometry nozzles.* 37th Aerospace Sciences Meeting and Exhibit. https://doi.org/10.2514/6.1999-365.

Muhammed, I. V. V., Banu, S. N., Suryan, A., Lijo, V., Simurda, D. & Kim, H. D. (2024). Computational study of flow separation in truncated ideal contour nozzles under high-altitude conditions. *International Journal of Fluid Engineering*, *1*(1), 013101. https://doi.org/10.1063/5.0190399

Neely, A. J., Gesto, F., & Young, J. 2007. *Performance studies of shock vector control fluidic thrust vectoring.* 43rd AIAA/ASME/SAE/ASEE Joint Propulsion Conference & Exhibit. https://doi.org/10.2514/6.2007-5086.

Reddy, K. P., Nair, C. G. S., & Biju, S. R. (2021). Systems engineering studies on induction of redundant electromechanical engine gimbal control actuation system in the second stage polar satellite launch vehicle. *Advances in Systems Engineering*, 609-618. https://doi.org/10.1007/978-981-15-8025-3.

Resta, E., Marsilio, R. & Ferlauto, M. (2021). Thrust vectoring of a fixed axisymmetric supersonic nozzle using the shock-vector control method. *MDPI Journal*, *6*(2), https://doi.org/10.3390/fluids6120441.

Salimi, M. R., Askari, R., & Hasani, M. (2022). Computational investigation of effects of side-injection geometry on thrust vectoring performance in a fuel-injected dual throat nozzle. *Journal of Applied Fluid Mechanics* *15*(4), 1137-1153. https://doi.org/10.47176/jafm.15.04.33354

Schwagerus, N., Soshel, M., Krummenauer, M., Kozulovic, D., & Niehuis, R. (2023). Numerical investigation of a Coandă-based fluidic thrust vectoring system for subsonic nozzles. *CEAS*

Aeronaut Journal, 14, 939–952. https://doi.org/10.1007/s13272-023-00677-8.

Shinde, R. M., & Singh, S. (2017). Automation in non-destructive examination for thrust chamber assembly of vikas engine. *Journal of Nondestructive Testing. 22*(6). https://www.ndt.net/?id=21244.

Tuttle, J. L., & Blount, D. H. (1983). *Perfect bell nozzle parametric and optimization curves*. NASA-RP-1104.

Wang Z., Feng, Y., Yang, Y., Wang, J., Xu, S. & Qin, J. (2024). Multi-objective optimization of rectangular cooling channel design using Design of Experiments (DOE). *Applied Thermal Engineering, 242*, 122507. https://doi.org/10.1016/j.applthermaleng.2024.122507.

Wing, D. J., Mills, C. T. L., & Mason, M. L. (1997). *Static investigation of a multi axis thrust- vectoring nozzle with variable internal contouring ability*. NASA TP-3628.

Wu, K. X., Kim, T. H., & Kim, H. D. (2021). Numerical study of fluidic thrust vector control using dual throat nozzle. *Journal of Applied Fluid Mechanics, 14*(1), 73-87. https://doi.org/10.47176/jafm.14.01.31690

Wu, K., Kim, T. H., & Kim, H. D. (2020a). Sensitivity analysis of counterflow thrust vector control with a three-dimensional rectangular nozzle. *Journal of Aerospace Engineering, 34*(1). https://doi.org/10.1061/(ASCE)AS.1943-5525.0001228.

Wu, K., Kim, T. H., & Kim, H. D. (2020b). Theoretical and numerical analyses of aerodynamic characteristics on shock vector control. *Journal Aerospace Engineering. 33*(5). https://doi.org/10.1061/(ASCE)AS.1943-5525.0001169.

Wu, K., Jin, Y. & Kim, H. D. (2019). Hysteretic behaviour in counter-flow thrust vector control. *Journal Aerospace Engineering, 32*(4). https://doi.org/10.1061/(ASCE)AS.1943-5525.0001027.

Yagle, P. J., Miller, D. N., Ginn, K. B. & Hamstra, J. W. (2001). Demonstration of fluidic throat skewing for thrust vectoring in structurally fixed nozzles. *Journal of Engineering Gas Turbines and Power, 123*(3), 502-507. https://doi.org/10.1115/1.1361109.

Yang, C., Yakawa, G., & Wu, C. C. (2000). Quadrilateral approaches for accurate free mesh method. *International Journal Numerical Methods in Engineering, 47*, 1445-1462. https://doi.org/10.1002/(SICI)10970207(20000320)47:8<1445::AID-NME838>3.0.CO;2-K.

Yu, B., & Shu, W. (2017). A novel control approach for a thrust vector system with electromechanical actuator. *IEEE Access, 5*, 15542–15550. https://10.1109/ACCESS.2017.2731779.

Yu, K., Yang, X., & Mo, Z. (2014). profile design and multifidelity optimization of solid rocket motor nozzle. *Journal of Fluids Engineering, 136*(3). https://doi.org/10.1115/1.4026248.

Zeng, L., Gao Z., Tiang, X., & Wang, L. (2024). Mechanism analysis of the vortex ring and its effects on an axial descending rotor. *International Journal of Fluid Engineering, 1*(2). https://doi.org/10.1063/5.0200688.

Zmijanovic, V., Leger, L., Lago, V., Sellam, M., & Chpoun, A. (2012). *Experimental and numerical study of thrust-vectoring effects by transverse gas injection into a propulsive axisymmetric c-d nozzle.* 48th AIAA/ASME/SAE/ASEE Joint Propulsion Conference & Exhibit. https://10.2514/6.2012-3874.